Interrelation between Ion-Intercalation and Structure in Prussian Blue Analogues

Masamitsu Takachi

February 2017

Interrelation between Ion-Intercalation and Structure in Prussian Blue Analogues

Masamitsu Takachi

Doctoral Program in Physics

Submitted to the Graduate School of

Pure and Applied Sciences

in Partial Fulfillment of the Requirements

for the Degree of Doctor of Philosophy in

Science

at the

University of Tsukuba

Contents

1 Introduction

1.1 Ion intercalation and structure
1.2 Objective of this thesis
1.3 Feature of Prussian blue analogues
1.4 Contents of this thesis

2 Experimental methods

2.1 Film preparation
2.2 SEM and AFM observation
2.3 Synchrotron-radiation X-ray powder diffraction
2.4 Electrochemical measurement
2.5 Complex impedance spectroscopy
    2.5.1 Randles equivalent circuit model
    2.5.2 Constant phase element (CPE)-restricted impedance
2.6 Microscopy system for recording images

3 Na^+ / Li^+ diffusion constant (D) vs. lattice constant a

3.1 Results
    3.1.1 Discharge curve of the films
    3.1.2 Complex impedance spectra
    3.1.3 Temperature dependence of complex impedance spectra
    3.1.4 Activation energy of D
3.2 Discussion
3.3 Summary

4 Na^+ / Li^+ diffusion constant (D) vs. ion concentration x

4.1 Results
4.1.1 Discharge curve of the films
4.1.2 Complex impedance spectra
4.1.3 Temperature dependence of complex impedance spectra
4.1.4 Activation energy of D and R_{ct}
4.2 Discussion
4.3 Summary

5 *In situ* microscopic observation in $Li_xCo[Fe(CN)_6]_{0.90}$

5.1 Results
5.1.1 Li^+ concentration x vs. visible absorption spectra
5.1.2 *In situ* microscopic observation (d = 1.5 μm)
5.1.3 Lattice constant a of green and black region
5.1.4 *In situ* microscopic observation (d = 0.5 μm)
5.1.5 Normalized absorption intensity against x
5.2 Discussion
5.3 Summary

6 Conclusion

Acknowledgements

References

Related publications of this thesis

1 Introduction

1.1 Ion intercalation and structure

The ion intercalation is the phenomena that guest ions such as Li^+ and Na^+ are inserted into the host compounds, and is utilized in lithium-ion secondary battery [1-4]. In this thesis, the ion intercalation is tentatively divided into the two processes, that is, ion insertion into the host compound and ion diffusion within the host compound. On the other hand, the structure is used in a rather wide sense, including the host structure, guest ion concentration, guest ion species, and spatial distribution of the valence of the transition metal.

The ion insertion is well known to influence the host structure. For example, removal of lithium ion from $LiFePO_4$ causes phase separation into $LiFePO_4$ and $FePO_4$ [5,6]. C. Delmas, *et al*. [7] experimentaly confirmed that individual particles in the phase separated region are essentially single phase, and they proposed domino-cascade model. N. Ohmer, *et al* . [8] performed *in situ* scanning transmission X-ray microscopy (STXM) measurments. They observed propagation of $LiFePO_4$ and $FePO_4$ in a μm scale along the (010) direction (Li diffusion direction).

On the other hand, the ion diffusion constant significantly depends on the structure, such as lattice constant, guest ion concentration, guest ion species. For example, H. Xia *et al*. [9] reported that the values $D^{Li}(= 10^{-13}\sim10^{-11}\mathrm{cm^2/s})$ of in Li_xCoO_2 with a layered rock-salt structure against Li^+ concentration range of $0.15 < x < 0.75$. The magnitude of D^{Li} increases with decrease x in the range of $0.5 < x < 0.75$. In this Li^+ concentration range, the interlayer distance (c-lattice parameter) increases with decreasing x. Van der Ven and Ceder [10,11] calculated the activation barrier of Li_xCoO_2 by first-principles calculations. They concluded that the activation barrier is sensitive to the Li^+ concentration because of the strongly varying c-lattice parameter of the host structure and the change in effective valence of the cobalt ions. T. Shibata, *et al*. [12] investigated that Na^+ diffusion constant and the activation energy against Na^+ concentration (x) in Na_xCoO_2. The magnitude of activation energy increases with increase in x. Here, we listed the ion diffusion constants of various compounds; $D^{Li} = 10^{-11}\sim10^{-10}\ \mathrm{cm^2/s}$ for $LiMn_2O_4$ [13] with a spinel structure, $10^{-15}\sim10^{-12}\ \mathrm{cm^2/s}$ for $LiFePO_4$ [14] with an olivine structure, $D^{Na} = \sim10^{-11}\mathrm{cm^2/s}$ for $NaCoO_2$ [12], and $\sim10^{-11}\mathrm{cm^2/s}$ for $NaMnO_2$ [15] with a layered rock-salt structure.

1.2 Objective of this thesis

The objective of this thesis is to clarify the interrelation between the ion intercalation and structure in Prussian blue analogues. In particular, we focused on the following interrelation, as schematically shown in Figure 1.1.

(I) ion diffusion and lattice constant

(II) ion diffusion and ion concentration and species

(III) ion insertion and spatial distribution of the valence of the transition metal

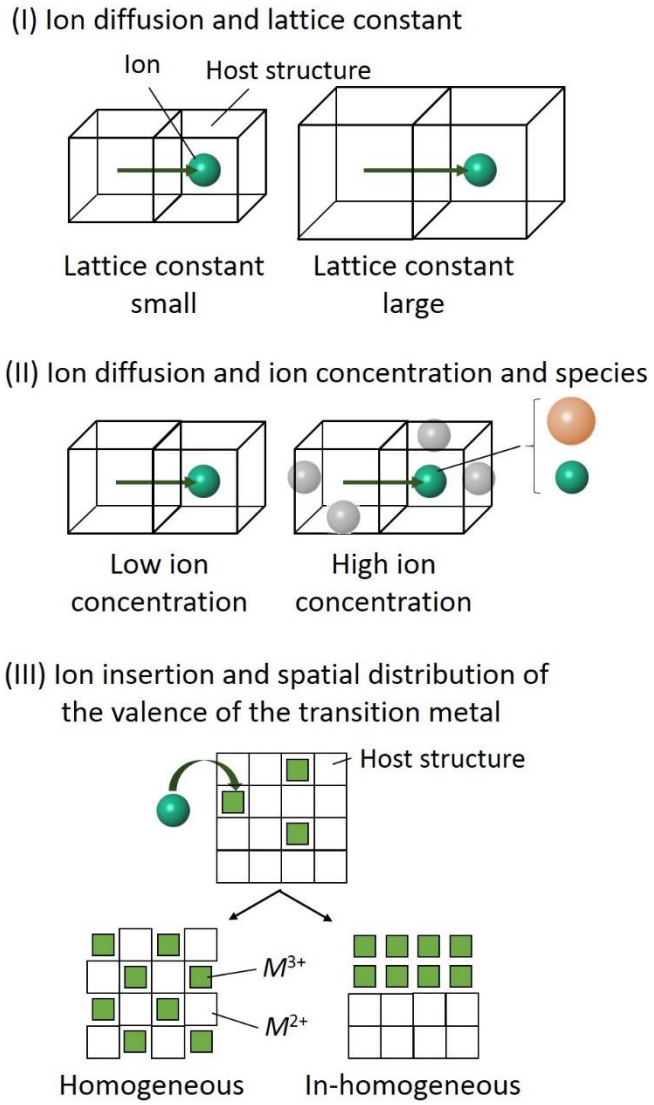

Figure 1.1 Schematic illustration of the interrelation between ion intercalation and structure, (I) ion diffusion and lattice constant, (II) ion diffusion and ion concentration and species, and (III) ion insertion and spatial distribution of the valence of the transition metal.

1.3 Feature of Prussian blue analogues

Prussian blue, chemical composition expressed as $Fe[Fe(CN)_6]_{0.75}$, was discovered as the first modern synthetic pigment by Diesbach in 1704. Prussian blue synthesized easily from ferrocyanide anions $[Fe(CN)_6]^{2-}$ and iron cations Fe^{3+}. When change Fe^{3+} to another transition metals, we can obtain valuable analogues. Figure 1.2 shows the schematic structure of Prussian blue analogues, $A_xM[Fe(CN)_6]_y\,zH_2O$ (A and M are an alkaline metal and transition metal, respectively). The compound belongs to NaCl type face-centered cubic lattice ($Fm\underline{3}m$; $Z = 4$) and shows a cyano-bridged three-dimensional framework, $-M-NC-Fe-CN-M-$. The nano-spaces of the framework can accommodate the alkaline metal ions, *e.g.*, Li^+, Na^+, K^+, Rb^+, Cs^+, Ca^{2+}, Mg^{2+}, and Sr^{2+} [16-18], or water molecules (zeolite waters). Some parts of the $[Fe(CN)_6]$ sites are vacant (defined as the amount of deficiency: y), and are replaced by the water molecules (ligand waters). A included in the framework can be intercalated by electrochemical method or by applying external voltage.

We have chosen Prussian blue analogues as the target material for the following reasons.

(a) their lattice constant can be finely controlled by the chemical substitution [19,20]

(b) they can accommodate both Li^+ and Na^+ in the same host [16-18,21-27]

(c) they show significant color change reflecting valence change [27]

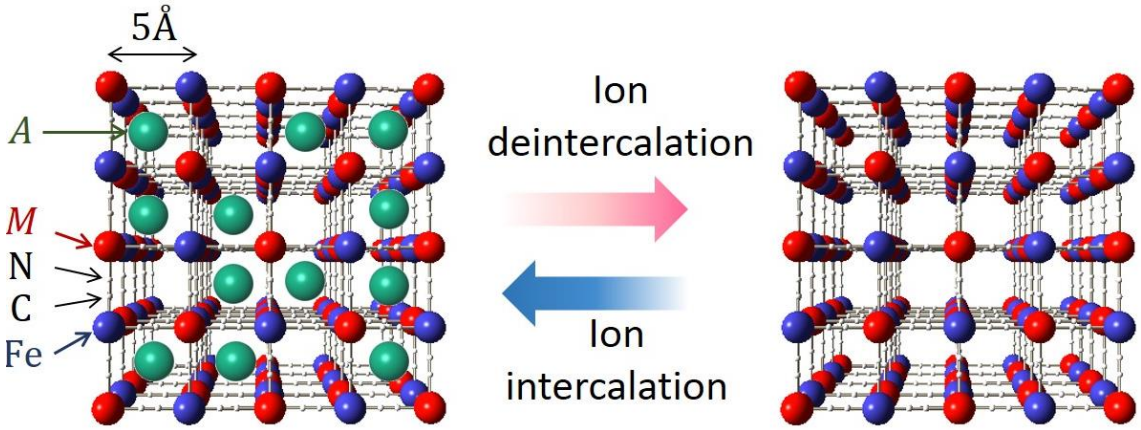

Figure 1.2 Schematic structure of Prussian blue analogues, $A_xM[Fe(CN)_6]_y\,zH_2O$ (A and M are an alkaline metal and transition metal, respectively). For simplicity, H_2O is omitted.

Y. Moritomo and H. Tanaka [20] reported that the framework size can be finely controlled by the substitution of transition metal (M). Figure 1.3 shows lattice constant (a) against ionic radius (r_M) of transition metal. The magnitude of a increases linearly with increase in r_M as a [nm] = 0.891 + $2r_M$[nm] in $(Cs,Rb)_xM[Fe^{3+}(CN)_6]_y$ (M = Co, Fe, Ni, Cu, Zn, Mn, and Cd). Furthermore, Y. Moritomo, *et. al.* [27] reported that thin film of $Li_xM[Fe(CN)_6]_yzH_2O$ (M= Ni, Co ,Mn, and Cd) show characteristic color change as shown in Figure 1.4. They suggested that it can be utilized as a charge indicator of secondary batteries.

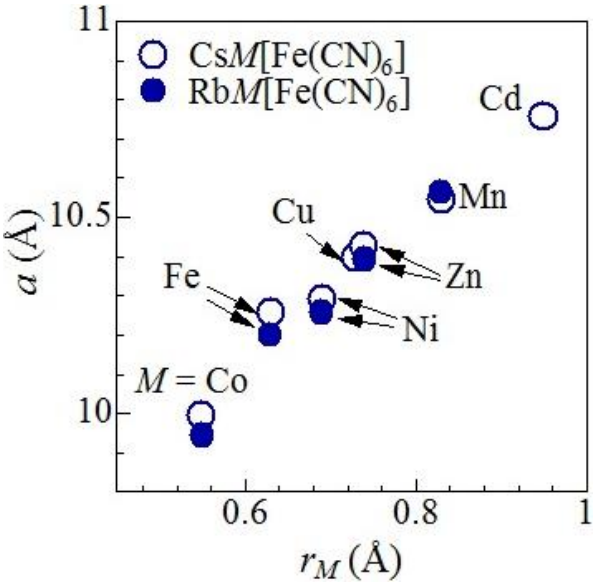

Figure 1.3 Lattice constant (a) against ionic radius (r_M) of transition metal in $(Cs,Rb)_xM^{2+}[Fe^{3+}(CN)_6]_y$ (M= Co, Fe, Ni, Cu, Zn, Mn, and Cd). Data were cited and modified from Ref. [19,20].

	M = Ni	M = Co	M =Mn	M = Cd
Full charge				
Full discharge				

Figure 1.4 Color change against charge / discharge process in $Li_xM[Fe(CN)_6]_y$ zH_2O (M= Ni, Co ,Mn, and Cd). Data were cited and modified from Ref. [27].

1.4 Contents of this thesis

This thesis consists of five chapters.

In chapter 1 (this chapter), we mentioned about the motivation and purpose of this thesis. We introduced the feature of Prussian blue analogues.

In chapter 2, we mentioned about experimental method. We explained the film preparation and characterization of them by SEM and AFM observation, Synchrotron-radiation X-ray powder diffraction, electrochemical measurement, and so on. We further explained details of the complex impedance spectroscopy and *in situ* microscopic observation system with use of a hand-made optical battery cell.

In chapter 3, we reported the diffusion constant D and activation energy E_a against lattice constant a. We discussed the interrelation between the ion diffusion constant and lattice constant.

In chapter 4, we reported the diffusion constant D and activation energy E_a against ion concentration and species in manganese Prussian blue analogues. We discussed the interrelation between the ion diffusion constant and ion concentration and species.

In chapter 5, we reported the *in situ* microscopic observation in cobalt Prussian blue analogues, $Li_xCo[Fe(CN)_6]_{0.90}$ thin film. We discussed the Li^+ insertion and spatial distribution of the valence of the transition metal. Importantly, we found a macroscopic (several tens of μm) phase separation into $Li_{1.6}Co^{2+}[Fe(CN)_6]_{0.90}$ and $Li_{0.6}Co^{3+}[Fe(CN)_6]_{0.90}$. We ascribed the macroscopic phase separation to the volume change between $Li_{1.6}Co[Fe(CN)_6]_{0.90}$ and $Li_{0.6}Co[Fe(CN)_6]_{0.90}$.

2 Experimental methods

2.1 Film preparation

Thin film of Prussian blue analogues $A_xM[Fe(CN)_6]_yzH_2O$ (A = Na, Li ; M = Cd, Mn, Co) were electrochemically synthesized on indium tin oxide (ITO) transparent electrode by electrochemical deposition method. Electrochemical deposition method has been used for the plating of metals and it enable us to synthesize thin film over the ITO transparent electrode. Electrochemical deposition system was consisted of standard electrode, counter electrode, and working electrode. We used these electrodes for a standard Ag / AgCl electrode, Platinum electrode, and ITO transparent electrode. Figure 2.1 shows electrochemical deposition system having by a three electrodes and a potentiostat. The ITO transparent electrode was cut out to a size of 4 cm × 5 cm with glass-cutter. The surface of ITO transparent electrode was purified by the electrolysis of water adding 0.1 mol/L nitric acid for several tens of seconds. During the synthesis, the aqueous solution was stirred with a rotor.

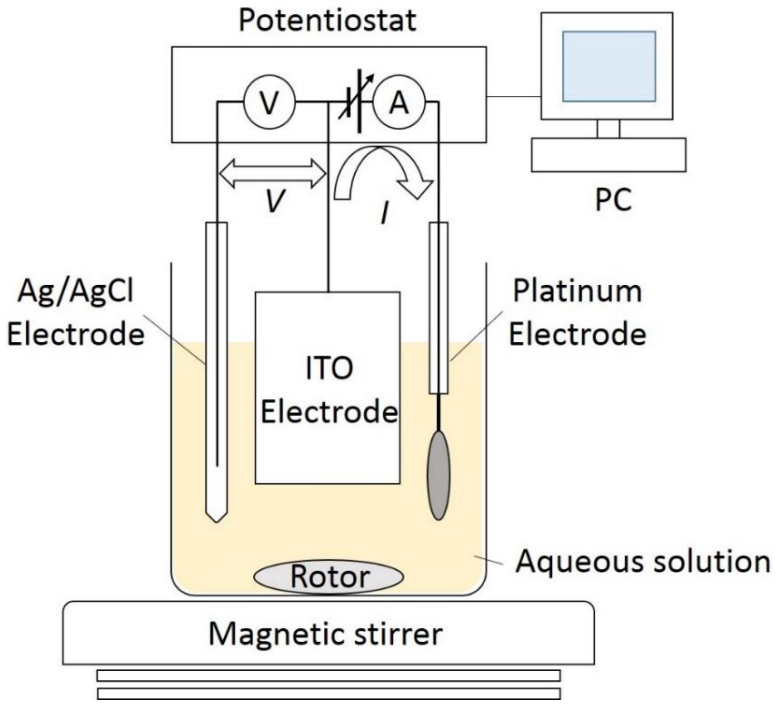

Figure 2.1 Schematic illustration of synthesizing film by electrochemical deposition. Electrochemical deposition system was consisted of standard Ag / AgCl electrode, Platinum electrode, and ITO transparent electrode.

The chemical composition of the films was determined by inductively coupled plasma (ICP) analysis (Nippon Jarrell-Ash ICAP-575 Emission Spectrometer) and CHN organic elementary analysis (Perkin-Elmer 2400 CHN elemental analyzer). ICP analysis is an analytical technique used for the detection of trace metals. CHN analysis is possible to determine the carbon (C), hydrogen (H), and nitrogen (N) elemental concentrations in a given sample. The elementary analysis of the films was performed at Chemical Analysis Division, Research Facility Center for Science and Engineering, University of Tsukuba.

$Na_{1.76}Cd[Fe(CN)_6]_{0.94}3.8H_2O$ (denoted as NCdF94) was synthesized under potentiostatic conditions in Table 1. As shown in Figure 2.2 (a), the film color of obtained NCdF94 is a transparent white. The chemical composition of the film was determined using result of ICP and CHN analysis. Calcd: Na,9.6; Cd,26.8; Fe,12.5; C,16.1; H,1.9; N,18.8%. Found: Na,10.3; Cd,27.0; Fe,13.1; C,15.8; H,1.8; N,17.9%. $Na_{1.36}Mn[Fe(CN)_6]_{0.84}3.4H_2O$ (denoted as NMnF84) was synthesized under potentiostatic conditions in Table 1. As shown in Figure 2.2 (b), the film color of obtained NMnF84 is a transparent white. The chemical composition of the film was determined using result of ICP and CHN analysis. Calcd: Na,9.7; Mn,16.9; Fe,14.5; C,18.7; H,2.1; N,21.8%. Found: Na,10.6; Mn,16.8; Fe,14.7; C,18.2; H,2.1; N,20.9%. $Na_{1.52}Co[Fe(CN)_6]_{0.88}3.1H_2O$ (denoted as NCoF88) was synthesized under potentiostatic conditions in Table 1. As shown in Figure 2.2 (c), the film color of obtained NCoF88 is a transparent green. The chemical composition of the film was determined using result of ICP and CHN analysis. Calcd: Na,10.4; Co,17.6; Fe,14.6; C,18.9; H,1.8; N,22.0%. Found: Na,11.2; Co,17.4; Fe,15.3; C,18.5; H,1.9; N,20.0%.

The thickness (d) of the films was controlled by the deposition time, and we prepared the films with $d \sim 500$ nm. The thickness of the films was determined by a stylus profilometer (Dektak3030). The active area of the film was determined by image analysis using ImageJ software. We evaluated the mass of films by using the film thickness, the film area, and the volume density. The volume density of films is experimentally determined and it's approximately 70 % against theoretical value.

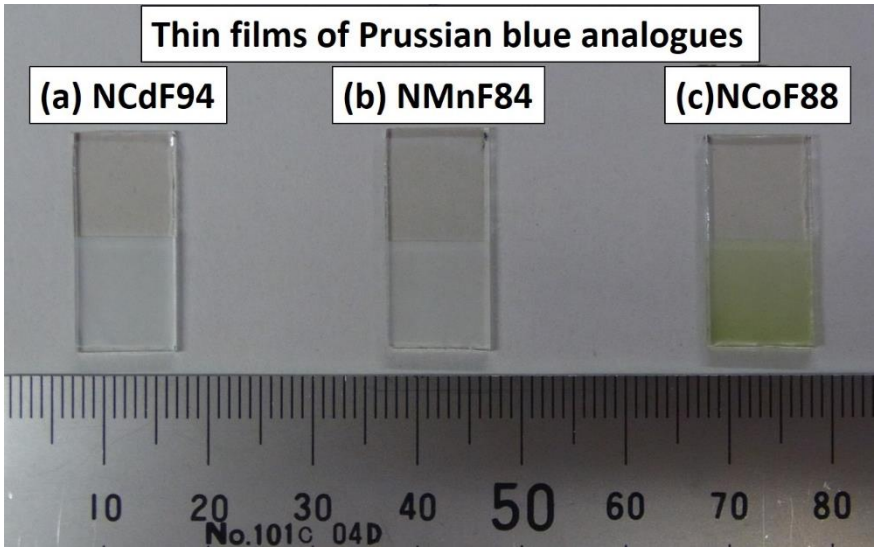

Figure 2.2 Picture of as-grown (a) $Na_{1.76}Cd[Fe(CN)_6]_{0.94}3.8H_2O$ (denoted as NCdF94), (b) $Na_{1.36}Mn[Fe(CN)_6]_{0.84}3.4H_2O$ (denoted as NMnF84), (c) $Na_{1.52}Co[Fe(CN)_6]_{0.88}3.1H_2O$ (denoted as NCoF88). Data were cited and modified from Ref. [28].

Table 1: The list of film conditions for each film.

Chemical composition	$Na_{1.76}Cd[Fe(CN)_6]_{0.94}$ $3.8H_2O$	$Na_{1.36}Mn[Fe(CN)_6]_{0.84}$ $3.4H_2O$	$Na_{1.52}Co[Fe(CN)_6]_{0.88}$ $3.1H_2O$
Abbreviation	NCdF94	NMnF84	NCoF88
Aqueous solution	1.0 mmol/L $K_3[Fe(CN)_6]$ 1.5 mmol/L $CdCl_2$ 1.0 mol/L NaCl	1.0 mmol/L $K_3[Fe(CN)_6]$ 1.5 mmol/L $MnCl_2$ 1.0 mol/L NaCl	0.8 mmol/L $K_3[Fe(CN)_6]$ 0.5 mmol/L $Co(NO_3)_2$ 5.0 mol/L $NaNO_3$
Applied potential (vs. Ag / AgCl)	saw tooth modulation between −0.8 and −0.1 V at 71 Hz	saw tooth modulation between −0.8 and −0.1 V at 71 Hz	saw tooth modulation between −0.8 and −0.1 V at 71 Hz
Synthesizing time	3 minnute	5 minnute	15 minnute
Film thickness	~ 500 nm	~ 500 nm	~ 500 nm

2.2 SEM and AFM observation

In order to investigate the surface morphologies of film, we observed scanning electron microscope (SEM) images and atomic force microscope (AFM) images. SEM measurements was performed with TECHNEX Mighty-8 at an acceleration voltage of 2keV. AFM measurements was performed with JEOL JSPM-5200 in the tapping mode. Figure 2.3 shows SEM images of as-grown $Na_{1.6}Co[Fe(CN)_6]_{0.90}2.9H_2O$ (denoted as NCoF90) film (a) $d = 1.5$ μm and (b) $d = 0.5$ μm. The NCoF90 film was used the microscopic observation experiment. The film thickness (d) was controlled by the deposition time. The grain size of the film were several hundred nm in both film.

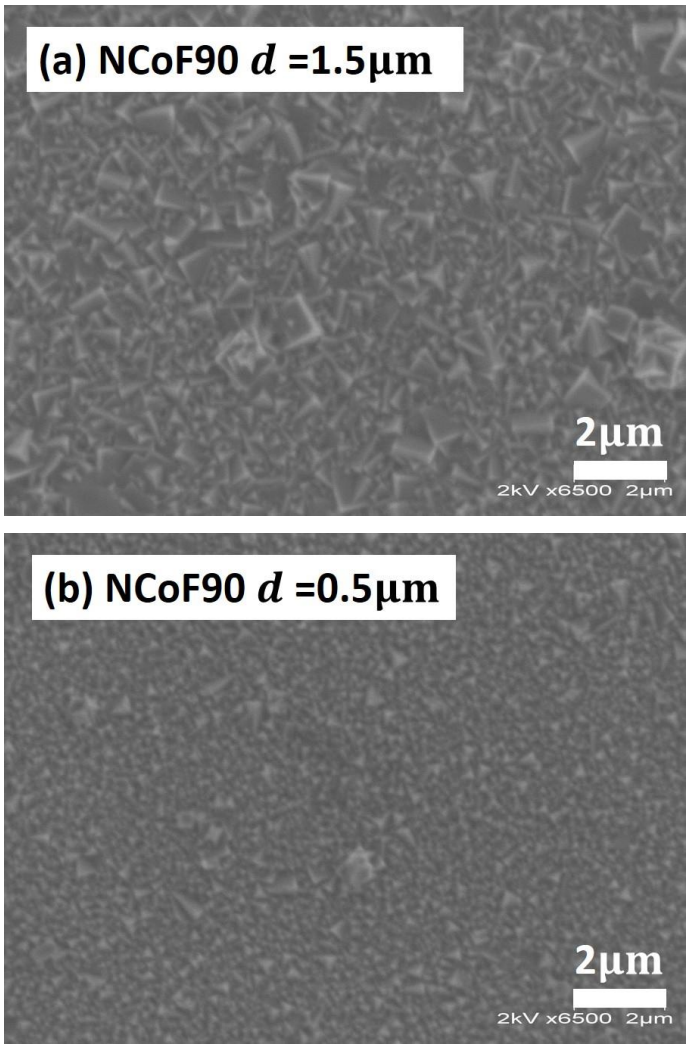

Figure 2.3 SEM images of as-grown NCoF90 film, (a) $d = 1.5$ μm and (b) $d = 0.5$ μm. Acceleration voltage was 2 keV.

Figure 2.4 shows AFM images of as-grown NCoF90 film (a) $d = 1.5$ μm and (b) $d = 0.5$ μm. The average roughness (R_a) are 46.6 nm for the $d = 1.5$ μm film and 34.1 nm for the $d = 0.5$ μm film.

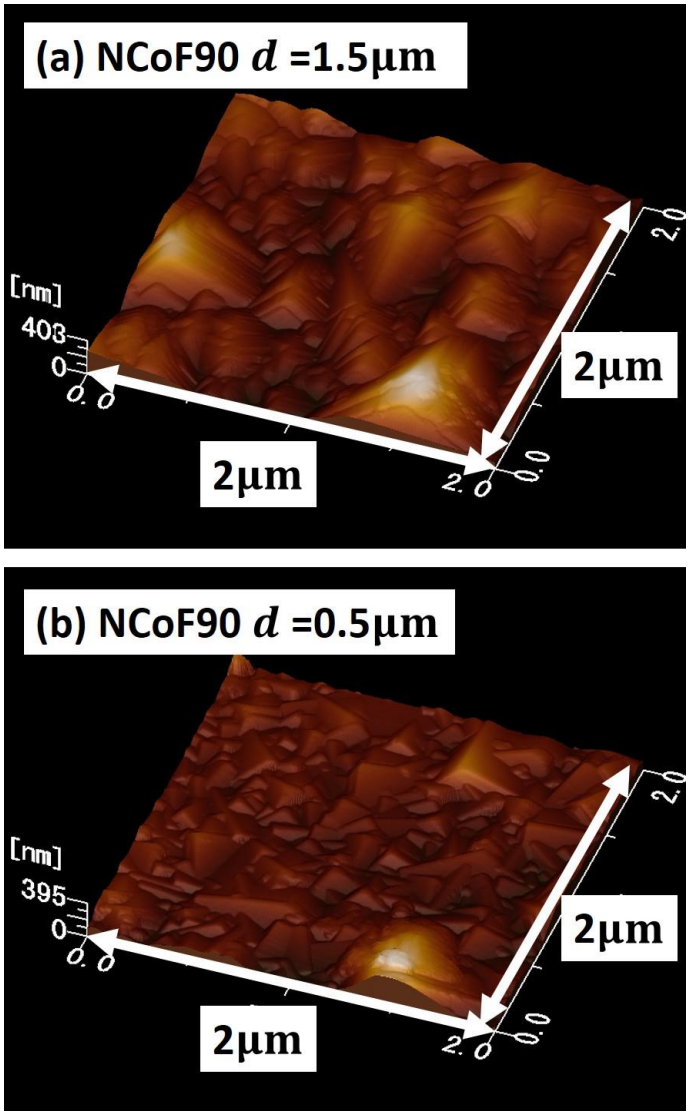

Figure 2.4 AFM images of as-grown NCoF90 film (a) $d = 1.5$ μm and (b) $d = 0.5$ μm. Measurement was performed in the tapping mode. The observation range was 2×2 μm^2 area.

2.3 Synchrotron-radiation X-ray powder diffraction

In order to investigate the structural characterization of the films, we measured X-ray powder diffraction patterns of as-grown NCdF94, NMnF84, and NCoF88 films. These films were carefully removed from the ITO transparent electrode with a microspatula, and then fine powders were put into 300 μmϕ glass capillaries under atmospheric conditions within a few minutes. Experiments were performed at BL8B beamline of Photon Factory, KEK. The wavelength of the X-ray (= 0.68799 Å) was calibrated by the lattice constant of standard CeO_2 powders.

Figure 2.5 shows X-ray powder diffraction patterns of as-grown NCdF94, NMnF84, and NCoF88. The magnitude of lattice constant a were refined by the Rietveld method with RIETAN-FP [29]. The NCdF94 belongs to the face-centered cubic model ($Fm\underline{3}m$; Z = 4) with lattice constant $a = 10.7113(9)$ Å. The NMnF84 belongs to the hexagonal model ($R\underline{3}m$; Z = 12) with lattice constant $a_H/\sqrt{2} = 10.602(7)$ Å, $c_H/\sqrt{3} = 10.421(1)$ Å. The NCoF88 belongs to the hexagonal model ($R\underline{3}m$; Z = 12) with lattice constant $a_H/\sqrt{2} = 10.514(1)$ Å, $c_H/\sqrt{3} = 10.084(1)$ Å.

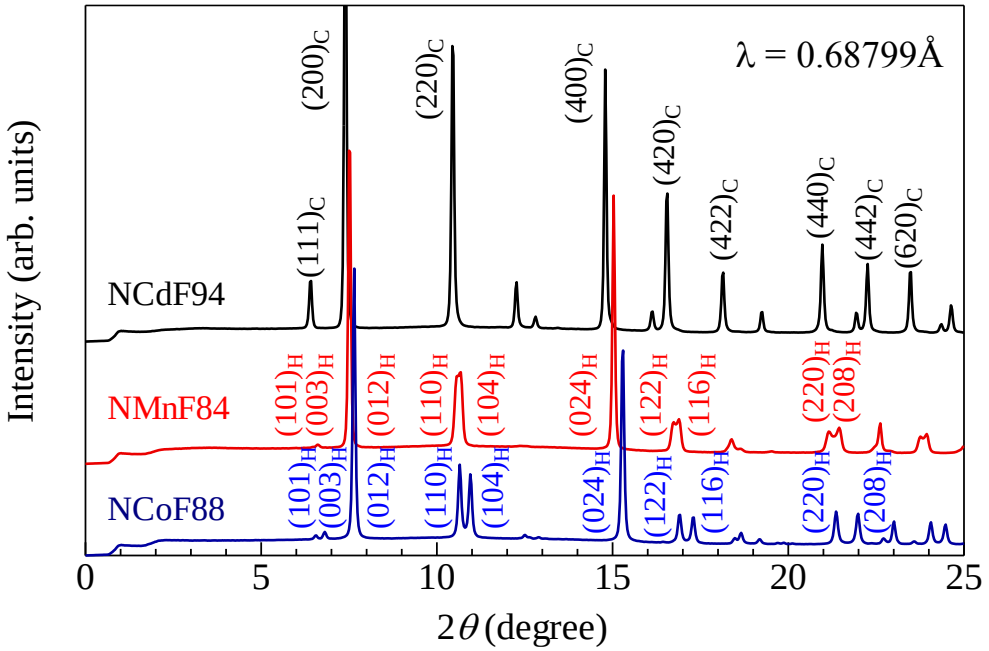

Figure 2.5 X-ray powder diffraction patterns of as-grown NCdF94, NMnF84, and NCoF88 films. X-ray wavelength was 0.68799 Å. In NCdF94, all the reflections can be indexed in the face-centered cubic ($Fm\underline{3}m$; Z = 4) setting. In NMnF84 and NCoF88, all the reflections can be indexed in the hexagonal ($R\underline{3}m$; Z = 12) setting. Data were cited and modified from Ref. [28].

2.4 Electrochemical measurement

In order to make the films controlled ion concentration x^{Na} / x^{Li}, we performed the charge / discharge measurement with a potentiostat (Hokuto Denko Co. Ltd.). Figure 2.6 shows schematic illustration of charge / discharge measurement by using a handmade beaker-type two-pole cell.

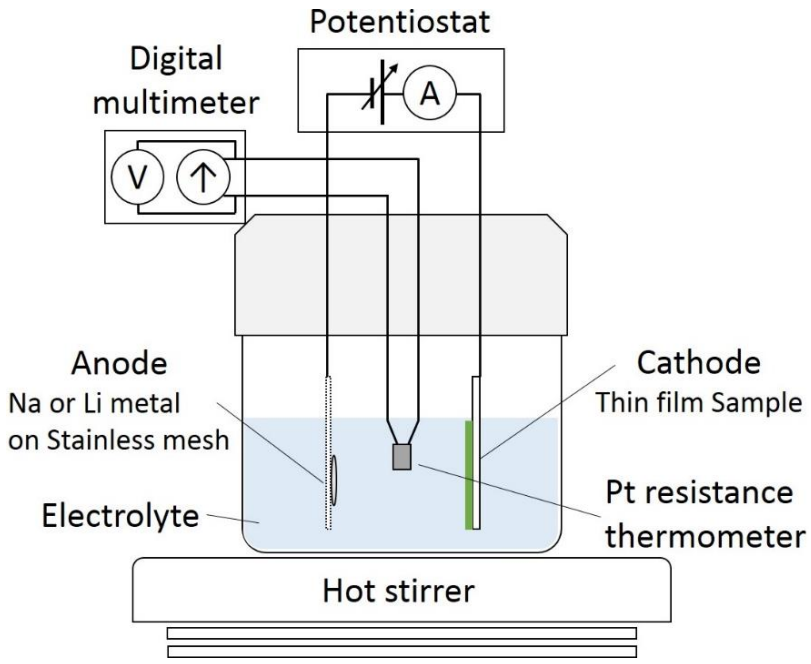

Figure 2.6 Schematic illustration of charge / discharge measurement by using a handmade beaker-type two-pole cell. The film and Na / Li metal were used as the cathode and anode, respectively.

In NCdF94, NMnF84, and NCoF88, the film and Na metal were used as the cathode and anode, respectively. The electrolyte was ethylene carbonate / diethyl carbonate (EC / DEC) containing 1 mol/L $NaClO_4$. The cut-off voltage was from 2.0 to 4.0 V and current rate was about 1 C. The active area of the film was about 1 cm^2. The measurement was performed under Argon (Ar atmosphere in an Ar filled glove box.

In LCdF94 and LMnF84, the film and Li metal were used as the cathode and anode, respectively. Na in the as-grown film was electrochemically substituted for Li. The electrolyte was ethylene carbonate / diethyl carbonate (EC / DEC) containing 1 mol/L $LiClO_4$. The cut-off voltage was from 2.0 to 4.2 V and current rate was about 1 C. The active area of the film was about 1 cm^2. The measurement was performed under Ar atmosphere in an Ar filled glove box.

Before complex impedance spectra (CIS) measurement, we performed charge / discharge measurement in a few cycles and checked whether the observed capacity of the film was close to the ideal capacity. The battery capacity [mAh/g] is expressed as the product of current (I) and time (t) per unit mass (m). We calculated the total amount of current required to complete full discharge. The experimental error for the mass and hence the observed capacity (Q_{obs}) is ~10%. We assumed that the amount of x in experimental discharge capacity is the amount of x_{ideal} in ideal discharge capacity, and ion concentration x gives the following form:

$$x = \frac{I \cdot t}{m} \times \frac{x_{\mathrm{ideal}}}{Q_{\mathrm{obs}}}$$

We measured CIS by potentiostatic impedance (PEIS) mode with a potentiostat (BioLogic SP-150). The PEIS experiment performs impedance measurement into potentiostatic mode by applying a sinus around a potential E that can be set to a fixed value or relatively to the cell equilibrium potential. Figure 2.7 shows the parameter setting window of potentiostat. The frequency range was from initial (f_{i}) 200 kHz to final (f_{f}) 5 mHz, and amplitude (V_{a}) was 30 mV. The frequencies distribution N_{d} between the scan bounds f_{i} and f_{f} was 10 points per decade. The temperature (T) dependence of CIS was measured with a Platinum resistance thermometer in the heating run. We conformed the temperature variation of CIS was recovered when the film was cooled to its initial temperature.

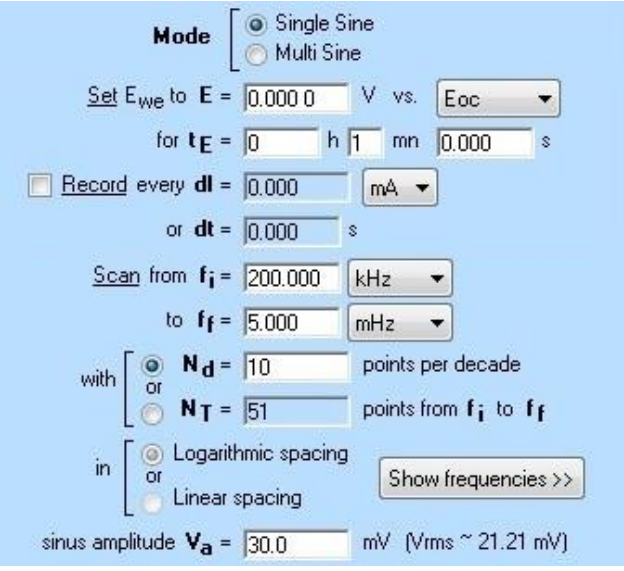

Figure 2.7 Parameter setting of PEIS mode. The frequency range was from initial (f_{i}) 200 kHz to final (f_{f}) 5 mHz, and amplitude (V_{a}) was 30 mV.

2.5 Complex impedance spectroscopy

2.5.1 Randles equivalent circuit model

Complex impedance spectroscopy (CIS) is one of the dynamical measurement methods. During the measurement, the redox reaction on electrode is shifted from the equilibrium state to the non-equilibrium state by giving some external signal. We can obtain information about the elementary process by analyzing the response in the relaxation process of redox reaction. CIS is usually measured by applying AC potential to the electrode and measuring the response current.

CIS data is commonly analyzed by fitting to an equivalent electrical circuit model. We analyzed the CIS with Randles equivalent circuit model which consists of electrolyte resistance (R_0), ionic charge-transfer resistance (R_{ct}), electric double-layer capacitance (C_{dl}), and ion diffusion impedance ($R_d \cdot \tilde{z}_d$: R_d and $\tilde{z}_d$ are characteristic resistance and ion diffusion impedance, respectively). Figure 2.8 shows schematic illustration of Randles equivalent circuit. Electrochemical impedance ($\tilde{Z}$) of Randles equivalent circuit including R_0, R_{ct}, C_{dl}, R_d, and $\tilde{z}_d$ gives the following form:

$$\tilde{Z} = R_0 + \frac{1}{i\omega C_{dl} + \frac{1}{R_{ct} + R_d \cdot \tilde{z}_d}} \qquad (1)$$

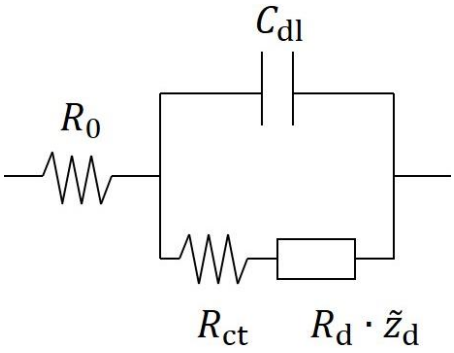

Figure 2.8 Randles equivalent circuit, which consists of electrolyte resistance (R_0), ionic charge-transfer resistance (R_{ct}), electric double-layer capacitance (C_{dl}), and ion diffusion impedance ($R_d \cdot \tilde{z}_d$: R_d and $\tilde{z}_d$ are characteristic resistance and ion diffusion impedance, respectively)

Figure 2.9 shows schematic illustration of the electrochemical reaction process. In general, the mass-transfer rate is slow compared to the charge-transfer rate. Thus, charge-transfer reaction is dominant in the high frequency region, and mass-transfer reaction is dominant in the low frequency region. We defined the critical frequency (f_c), and f_c^{-1} is the characteristic time when the diffusion length of ion reaches the film thickness d. The diffusion constant D is roughly evaluated as $D = 2\pi f_c d^2$.

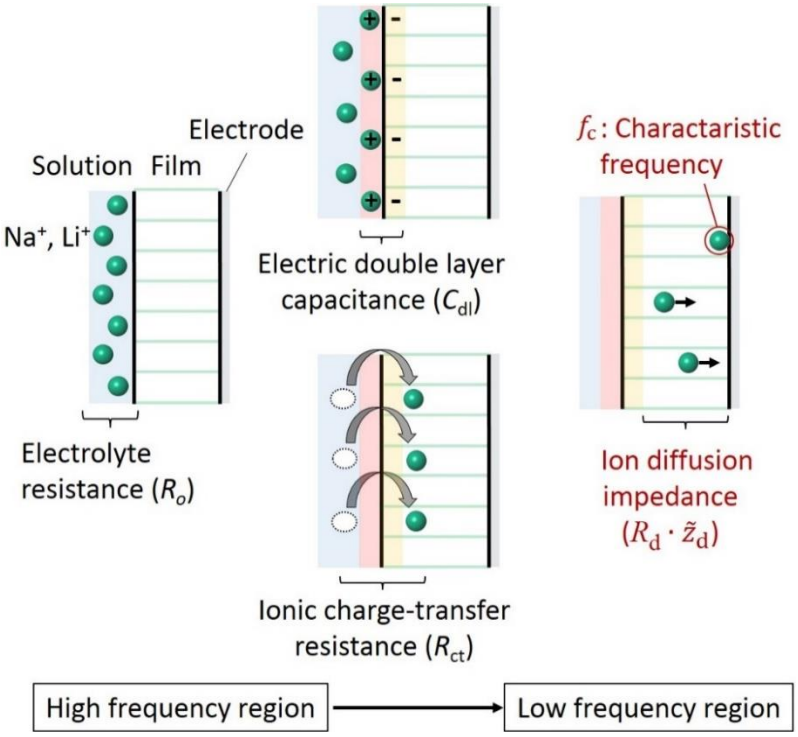

Figure 2.9 Schematic illustration of electrochemical reaction process.

At the film / electrode boundary, the boundary condition is $|\tilde{z}_d| = \infty$ ($\because f \to 0$). The film / electrode boundary condition means that ions don't diffuse in the film anymore. Then, ion diffusion impedance ($\tilde{z}_d$) gives the following form:

$$\tilde{z}_d(u) = \frac{1}{\sqrt{u}} \coth \sqrt{u}, \qquad u = \frac{i\omega d^2}{D} \qquad (2)$$

where $\omega (= 2\pi f)$, d, and D are the angular velocity, film thickness, and diffusion constant, respectively. The properties of equation (2) are well known, the point of $|u| = 2\pi$ that correspond to the frequency f_c marks the separation between two distinct. For $|u| \gg 2\pi$, $\tilde{z}_d(u)$ behaves straight lines with the angle of $\pi/4$ against the real axis, it is called "Warburg impedance". For $|u| \ll 2\pi$, $\tilde{z}_d(u)$ diverge perpendicular to the real axis.

Figure 2.10 shows (a) the result of CIS calculation using the formula (1) and (2), (b) schematic illustration of film / electrode boundary. The parameter values are as follows; $R_0 = 100\,\Omega$, $R_{ct} = 100\,\Omega$, $C_{dl} = 1.5\times10^{-5}$ F, $R_d = 100\,\Omega$, $D = 2.5\times10^{-10}$ cm^2/s, $d = 500$ nm. In the high frequency region, the CIS show semicircle due to R_0, R_{ct} and C_{dl}. With the decrease in the frequency f, the CIS form straight lines with the angle of $\pi/4$ against the real axis. With further decrease in the frequency f, the CIS diverge perpendicular to the real axis.

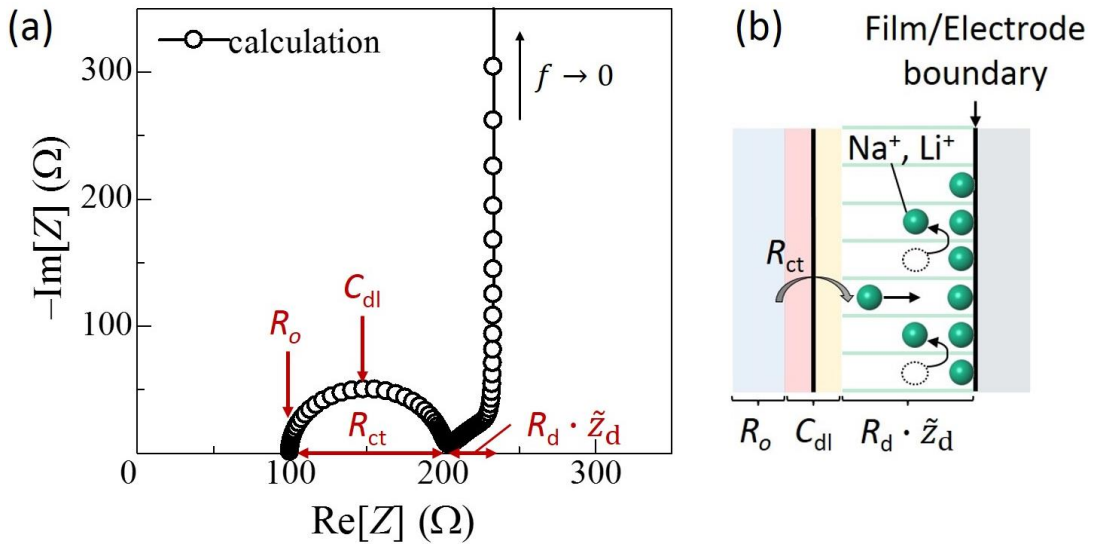

Figure 2.10 (a) The result of CIS calculation (parameter values: $R_0 = 100\,\Omega$, $R_{ct} = 100\,\Omega$, $C_{dl} = 1.5\times10^{-5}$ F, $R_d = 100\,\Omega$, $D = 2.5\times10^{-10}$ cm^2/s, $d = 500$ nm), (b) schematic illustration of film / electrode boundary.

2.5.2 Constant phase element (CPE)-restricted impedance

The experimental data of CIS in low frequency region cannot often be fitted by using equation (2). The CIS in the low frequency region behaves the finite slope to the real axis. The finite slope to the real axis is ascribed to the different state of ion diffusion near the film / electrode boundary. In order to reproduce the finite slope in the low frequency region, we used the constant phase element (CPE)-restricted impedance [30]. At the film / electrode boundary, the boundary condition is $\tilde{z}_{\mathrm{d}} = {}^{1}/_{\alpha}\, u^{-n}$. Then, ion diffusion impedance ($\tilde{z}_{\mathrm{d}}$) gives the following form:

$$\tilde{z}_{\mathrm{d}}(u) = \frac{\alpha u^{n} + \sqrt{u}\coth\sqrt{u}}{u + \alpha u^{n+\frac{1}{2}}\coth\sqrt{u}}, \quad u = \frac{i\omega d^{2}}{D} \qquad (3)$$

where α and n are the dimensionless quantity and specific exponent, respectively. The specific exponent n is less than one. Equation (2) is obtained by assign $\alpha = 0$ to the equation (3). Figure 2.11 shows (a) the result of CIS calculation using the formula (1) and (3), (b) schematic illustration of film / electrode boundary. The parameter values are as follows; $R_0 = 100\ \Omega$, $R_{\mathrm{ct}} = 100\ \Omega$, $C_{\mathrm{dl}} = 1.5\times10^{-5}$ F, $R_{\mathrm{d}} = 100\ \Omega$, $D = 2.5\times10^{-10}\ \mathrm{cm^2/s}$, $d = 500$ nm, $\alpha = 0.8$, $n = 0.8$. In the high frequency region, the CIS show semicircle due to R_0, R_{ct} and C_{dl}. With the decrease in the frequency f, the CIS form straight lines with the angle of $\pi/4$ against the real axis. With further decrease in the frequency f, the CIS shows the finite slope to the real axis.

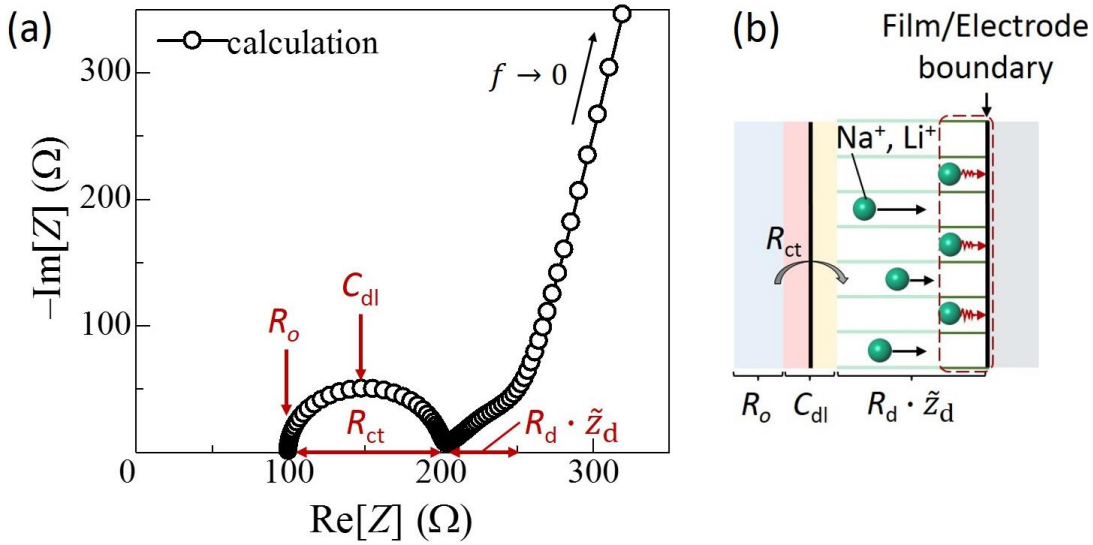

Figure 2.11 (a) The result of CPE calculation (parameter values: $R_0 = 100\ \Omega$, $R_{\mathrm{ct}} = 100\ \Omega$, $C_{\mathrm{dl}} = 1.5\times10^{-5}$ F, $R_{\mathrm{d}} = 100\ \Omega$, $D = 2.5\times10^{-10}\ \mathrm{cm^2/s}$, $d = 500$ nm, α=0.8, n=0.8.), (b) schematic illustration of film / electrode boundary.

We evaluated seven parameters R_0, R_{ct}, C_{dl}, Z_d, α, n and D by least squares fittings of the CIS. The observed CIS ($\widetilde{Z^{obs}}(f)$) and calculated CIS ($\widetilde{Z^{calc}}(f_j)$), j = 1,2, …. N), we defined the summed square of residuals;

$$S = \sum_{j=1}^{N} \left| \widetilde{Z^{obs}}(f) - \widetilde{Z^{calc}}(f_j) \right|^2$$

where N is the number of data points included in the fitting and S is the sum of squares error estimate. We calculated to find seven values (R_0, R_{ct}, C_{dl}, Z_d, α, n and D) that minimize the error S by making macro file in Excel.

2.6 Microscopy system for recording images

We made the optical battery cell which has a structure of cathode / Teflon sheet with square hole / anode as shown in Figure 2.12. The cathode and anode were $Li_{1.60}Co[Fe(CN)_6]_{0.90}2.9H_2O$ (Na was substituted for Li with electrochemical method in NCoF90, and denoted as LCoF90) film and Cu foil electrode attached with a small piece of Li metal. The hole of the Teflon sheet was filled with electrolyte. The electrolyte was ethylene carbonate / diethyl carbonate (EC / DEC) containing 1 mol/L $LiClO_4$. The battery cell assembled under Ar atmosphere in an Ar filled glove box and sealed with a clip. The charge / discharge behavior of the cell was stable and consistent literature [24] under air atmosphere at least ten hours. It is difficult to evaluate the current and the capacity due to bubble of Ar gas inevitably got in the square hole. Actually, some parts of the LCoF90 film remain unchanged during the charge / discharge process. For this reason, we assume that the fully-charged and fully-discharged state as $x = 0.0$ and $x = 1.6$, respectively.

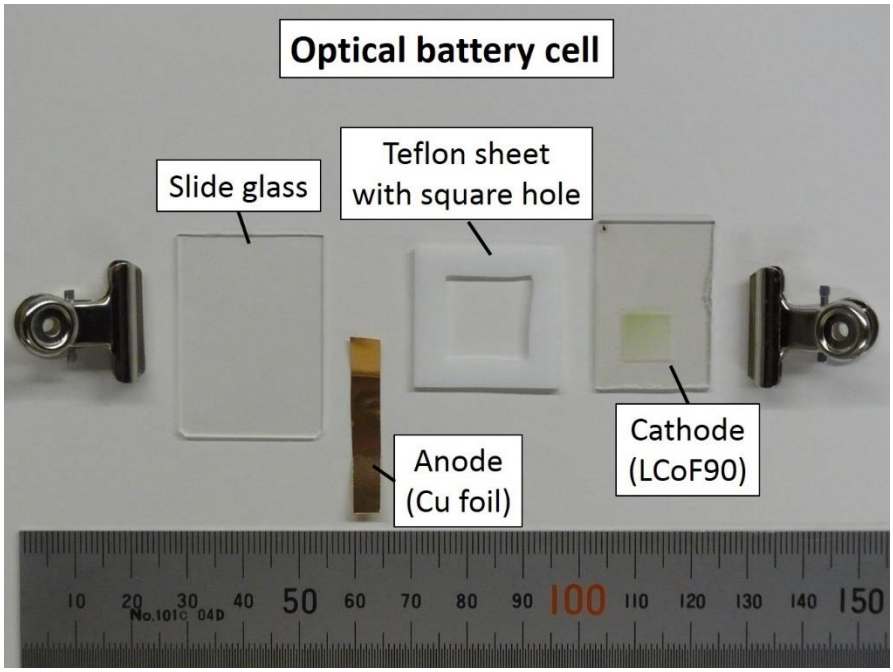

Figure 2.12 Picture of optical battery cell, which consists of cathode ($Li_{1.60}Co[Fe(CN)_6]_{0.90}2.9H_2O$ film), Teflon sheet with square hole, anode (Cu foil), slide-glass, and clips.

The *in-situ* microscopic images was recorded with a microscopy system equipped with a charge-coupled device (CCD) camera as shown Figure 2.13. The LED white light source was monochromized with a dichroic filter (DIF-50S-GRE: Sigma Kouki, Co Ltd.). The transmission range of the filter is 515-560 nm. The CCD image of transmission type diffraction grating film (500GPM: Edmund Optics, Co Ltd) are shown in Figure 2.14. The grating frequency was 500 lines per millimeter, thus, interval of bright line was 2μm. The size of the image was a vertical and horizontal 50 μm × 130 μm, the spatial resolution of the system was 1 μm.

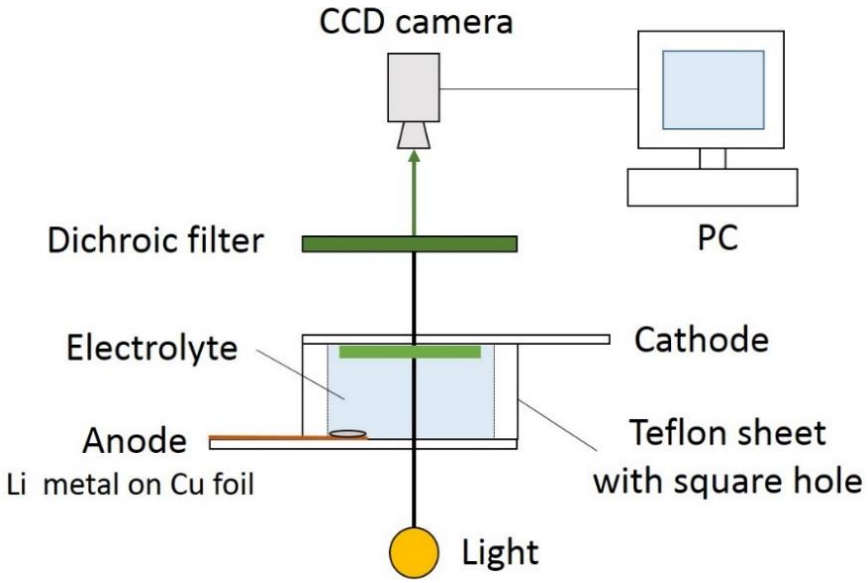

Figure 2.13 Schematic illustration of experimental set up for *in situ* microscopic observation.

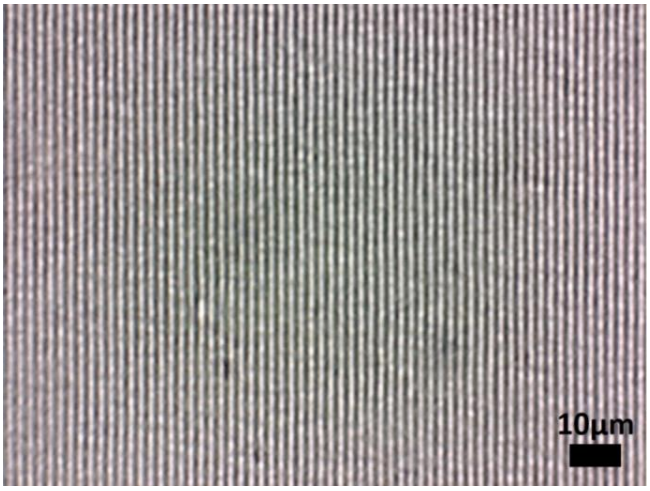

Figure 2.14 CCD image of transmission type diffraction grating film. The interval of bright line was 2 μm.

3 Na^+ / Li^+ diffusion constant (D) vs. lattice constant a

3.1 Results

3.1.1 Discharge curve of the films

In order to prepare the films controlled ion concentration x, we performed charge / discharge measurement with a potentiostat. Figure 3.1 shows discharge curves of (a) NCdF94, (b) NMnF84, and (c) NCoF88 films. The discharge curve can be regarded as the open-circuit-voltage (OCV) curve, because no current rate dependence was observed in this rate region. The film and Na metal were used as the cathode and anode, respectively. The electrolyte was ethylene carbonate / diethyl carbonate (EC / DEC) containing 1 mol/L $NaClO_4$.

In NCdF94, the discharge curve exhibits single plateau (I) measured at 0.8 C (see Figure 3.1 (a)). The observed discharge capacity (= 50 mAh/g) of NCdF94 was close to the ideal capacity (= 55 mAh/g) for the Na^+ intercalation from $x = 0.82$ to 1.76. In NMnF84, the discharge curve exhibits two plateau (I) and (II) measured at 0.8 C (see Figure 3.1 (b)). The observed discharge capacity (= 100 mAh/g) of NMnF84 was close to the ideal capacity (= 112 mAh/g) for the Na^+ intercalation from $x = 0.0$ to 1.36. In NCoF88, the discharge curve exhibits two plateau (I) and (II) measured at 1.1 C (see Figure 3.1 (c)). The observed discharge capacity (= 140 mAh/g) of NCoF88 was close to the ideal capacity (= 125 mAh/g) for the Na^+ intercalation from $x = 0.0$ to 1.52.

The valence states of transition metal were determined by X-ray absorption spectroscopy (XAS) measurement around the Cd, Mn, Co, and Fe K-edges. For NCdF94, we used the XAS data of the Li^+ substituted LCdF94. In plateau (I) of NCdF94, Fe K-edge spectra shows a slight shift with increase in x while Cd K-edge spectra does not change [27]. Thus, plateau (I) of NCdF94 can be ascribed to the reduction of Fe. In plateau (I) of NMnF84, Mn K-edge spectra shows a clearly change with increase in x while Fe K-edge spectra does not shift. In contrast, Fe K-edge spectra shows a slight shift while Mn K-edge spectra does not change in plateau (II) [31]. Thus, plateaus (I) and (II) of NMnF84 can be ascribed to the reduction of Mn and Fe, respectively. In plateau (I) of NCoF88, Fe K-edge spectra shows a slight shift with increase in x while Co K-edge spectra does not change. In contrast, Co K-edge spectra shows a clearly change while Fe K-edge spectra does not change in plateau (II) [26]. Thus, plateaus (I) and (II) of NCoF88 can be ascribed to the reduction of Fe and Co, respectively.

We listed discharge voltage (V) vs Na metal, electronic configuration, and redox site of the respective plateaus of each film in Table 2.

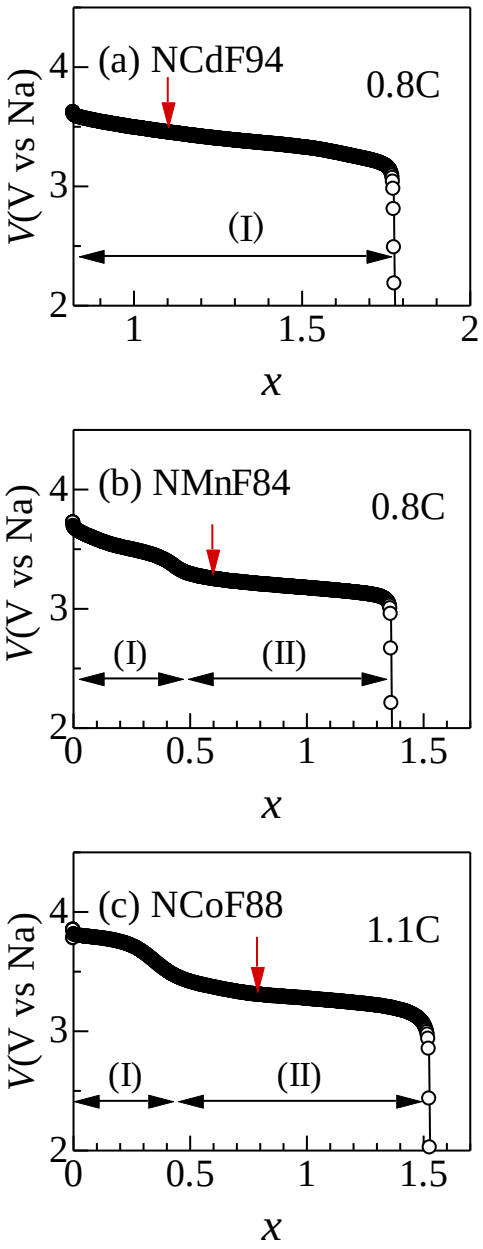

Figure 3.1 Discharge curves of (a) NCdF94, (b) NMnF84, (c) NCoF88 films. In NCdF94, the redox site of plateau (I) is Fe. In NMnF84, the redox site of plateau (I) and (II) are Mn and Fe, respectively. In NCoF88, the redox site of plateau (I) and (II) are Fe and Co, respectively. Red arrows in the figure indicate the position where CIS were measured. Data were cited and modified from Ref. [28].

Table 2: The list of discharge voltage (V) vs Na metal, electronic configuration, and redox site of the respective plateaus for each film.

	$Na_{1.76}Cd[Fe(CN)_6]_{0.94}3.8H_2O$ (NCdF94)		
Plateau	V (V vs Na metal)	Configuration	Redox site
I	~3.3	$Cd^{2+} - Fe^{2+\delta}$	Fe [27]

	$Na_{1.36}Mn[Fe(CN)_6]_{0.84}3.4H_2O$ (NMnF84)		
Plateau	V (V vs Na metal)	Configuration	Redox site
I	~3.5	$Mn^{2+\delta} - Fe^{3+}$	Mn [31]
II	~3.2	$Mn^{2+} - Fe^{2+\delta}$	Fe [31]

	$Na_{1.52}Co[Fe(CN)_6]_{0.88}3.1H_2O$ (NCoF88)		
Plateau	V (V vs Na metal)	Configuration	Redox site
I	~3.8	$Co^{3+} - Fe^{2+\delta}$	Fe [26]
II	~3.4	$Co^{2+\delta} - Fe^{2+}$	Co [26]

Here, we assumed the ideal redox reactions of each film from the result of the XAS measurement. The ideal redox reactions of (a) NCdF94, (b) NMnF84, and (c) NCoF88 are as follows;

(a) Redox reactions of NCdF94

Plateau (I)

$0.94Na^+ + Na_{0.82}Cd^{2+}[Fe^{3+}(CN)_6]_{0.94} \rightarrow Na_{1.76}Cd^{2+}[Fe^{2+}(CN)_6]_{0.94}$

(b) Redox reactions of NMnF84

Plateau (I)

$1.36Na^+ + Mn^{3+}_{0.52}Mn^{2+}_{0.48}[Fe^{3+}(CN)_6]_{0.84} \rightarrow 0.84Na^+ + Na_{0.52}Mn^{2+}[Fe^{3+}(CN)_6]_{0.84}$

Plateau (II)

$0.84Na^+ + Na_{0.52}Mn^{2+}[Fe^{3+}(CN)_6]_{0.84} \rightarrow Na_{1.36}Mn^{2+}[Fe^{2+}(CN)_6]_{0.84}$

(c) Redox reactions of NCoF88

Plateau (I)

$1.52Na^+ + Co^{3+}[Fe^{3+}(CN)_6]_{0.52}[Fe^{2+}(CN)_6]_{0.36} \rightarrow Na^+ + Na_{0.52}Co^{3+}[Fe^{2+}(CN)_6]_{0.88}$

Plateau (II)

$Na^+ + Na_{0.52}Co^{3+}[Fe^{2+}(CN)_6]_{0.88} \rightarrow Na_{1.52}Co^{2+}[Fe^{2+}CN)_6]_{0.88}$

Figure 3.2 shows discharge curves of (a) LCdF94 and (b) LMnF84 films. The film and Li metal were used as the cathode and anode, respectively. The electrolyte was ethylene carbonate / diethyl carbonate (EC / DEC) containing 1 mol/L $LiClO_4$.

In LCdF94, the discharge curve exhibits single plateau (I) measured at 0.8 C (see Figure 3.2 (a)). The observed discharge capacity (= 63 mAh/g) of LCdF94 was close to the ideal capacity (= 56 mAh/g) for the Li^+ intercalation from $x = 0.0$ to 0.94. In LMnF84, the discharge curve exhibits two plateau (I) and (II) measured at 1.4 C (see Figure 3.2 (b)). The observed discharge capacity (= 95 mAh/g) of LMnF84 was close to the ideal capacity (= 119 mAh/g) for the Li^+ intercalation from $x = 0.0$ to 1.36.

The valence states of transition metal were determined by the X-ray absorption spectroscopy (XAS) measurement around the Cd, Mn, and Fe K-edges. In plateau (I) of LCdF94, Fe K-edge spectra shows a slight shift with increase in x while Cd K-edge spectra does not change [27]. Thus, plateau (I) of LCdF94 can be ascribed to the reduction of Fe. In plateau (I) of LMnF84, Mn K-edge spectra shows a clearly change with increase in x while Fe K-edge spectra does not shift. In contrast, Fe K-edge spectra show a slight shift while Mn K-edge spectra does not change in plateau (II) [22]. Thus, plateaus (I) and (II) of LMnF84 can be ascribed to the reduction of Mn and Fe, respectively. We listed discharge voltage (V) vs Li metal, electronic configuration, and redox site of the respective plateaus of each film in Table 3.

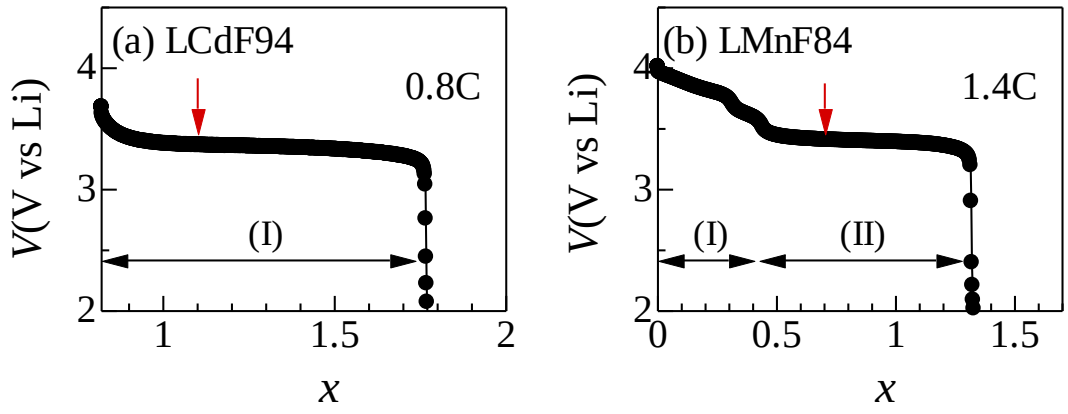

Figure 3.2 Discharge curves of (a) LCdF94 and (b) LMnF84 films. The redox of NCdF90 in plateau (I) is Fe. The redox of NMnF84 in plateau (I), (II) are Mn and Fe, respectively. Red arrows in the figure indicate the position where CIS were measured. Data were cited and modified from Ref. [28].

Table 3: The list of discharge voltage (V) vs Li metal, electronic configuration, and redox site of the respective plateaus for each film.

	$Li_{0.94}\ Na_{0.82}Cd[Fe(CN)_6]_{0.94}3.8H_2O$ (LCdF94)		
Plateau	V (V vs Li metal)	Configuration	Redox site
I	~3.3	$Cd^{2+} - Fe^{2+\delta}$	Fe [27]

	$Li_{1.36}Mn[Fe(CN)_6]_{0.84}3.4H_2O$ (LMnF84)		
Plateau	V (V vs Li metal)	Configuration	Redox site
I	~3.7	$Mn^{2+\delta} - Fe^{3+}$	Mn [22]
II	~3.3	$Mn^{2+} - Fe^{2+\delta}$	Fe [22]

Here, we assumed the ideal redox reactions of each film from the result of the XAS measurement. The ideal redox reactions of (a) LCdF94 and (b) LMnF84 are as follows;

(a) Redox reactions of LCdF94

Plateau (I)

$0.94Li^+ + Na_{0.82}Cd^{2+}[Fe^{3+}(CN)_6]_{0.94} \rightarrow Li_{0.94}\ Na_{0.82}Cd^{2+}[Fe^{2+}(CN)_6]_{0.94}$

(b) Redox reactions of LMnF84

Plateau (I)

$1.36Li^+ + Mn^{3+}{}_{0.52}Mn^{2+}{}_{0.48}[Fe^{3+}(CN)_6]_{0.84} \rightarrow 0.84Li^+ + Li_{0.52}Mn^{2+}[Fe^{3+}(CN)_6]_{0.84}$

Plateau (II)

$0.84Li^+ + Li_{0.52}Mn^{2+}[Fe^{3+}(CN)_6]_{0.84} \rightarrow Li_{1.36}Mn^{2+}[Fe^{2+}(CN)_6]_{0.84}$

3.1.2 Complex impedance spectra

In order to investigate Na^+ / Li^+ diffusion constant (D), we measured complex impedance spectra (CIS). Figure 3.3 shows the CIS of (a) NCdF94, NMnF84, and NCoF88 films against Na metal at 305K, the CIS of (b) LCdF94 and LMnF84 films against Li metal at 305 K. The CIS of plateau (I) regions were too deformed to analyze in NMnF84 (LMnF84) and NCoF88 films. Thus, we chose the plateau (II) for measurement in those films. The frequency range was from 200 kHz to 5 mHz. Arrows in the figure indicate the frequencies. Broken straight lines are guided to the eye. Solid curves are results of the least-squares fittings with the Randles equivalent circuit model.

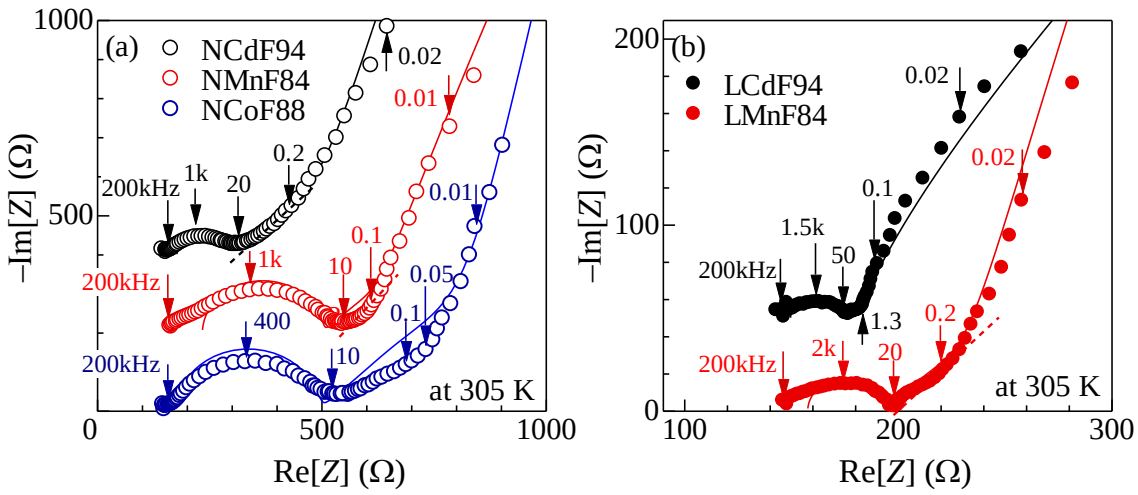

Figure 3.3 Complex impedance spectra of (a) NCdF94, NMnF84, and NCoF88 films at 305 K, (b) LCdF94 and LMnF84 films at 305 K. The frequency range was from 200 kHz to 5 mHz. Arrows in the figure indicate the frequencies. Broken straight lines are guided to the eye. Solid curves are results of the least squares fittings with the Randles equivalent circuit model. Data were cited and modified from Ref. [28].

In the high frequency region, the spectra shows semicircle due to ionic charge-transfer resistance (R_{ct}) and electric double-layer capacitance (C_{dl}). Ionic charge-transfer resistance of NCdF94 ($R_{\mathrm{ct}} = 115\ \Omega$) was much smaller than that of NMnF84 ($R_{\mathrm{ct}} = 272\ \Omega$) and NCoF88 ($R_{\mathrm{ct}} = 295\ \Omega$). On the other hand, electric double-layer capacitance (C_{dl}) was almost the same of all films, NCdF94 ($C_{\mathrm{dl}} = 1.7\times10^{-6}$ F), NMnF84 ($C_{\mathrm{dl}} = 1.5\times10^{-6}$ F), and NCoF88 ($C_{\mathrm{dl}} = 1.2\times10^{-6}$ F). The squashed semicircle of LCdF94 and LMnF84 films make it difficult to precisely evaluate R_{ct} and C_{dl}.

With decrease in f, the CIS form straight lines with the angle of $\pi/4$ against the real axis (broken straight line). With further decrease in f, the CIS deviate from the broken line. We evaluated the critical frequency f_c of NCdF94 ($f_{\mathrm{c}} = 0.19\ \mathrm{s}^{-1}$), NMnF84 ($f_{\mathrm{c}} = 0.10\ \mathrm{s}^{-1}$) and NCoF88 ($f_{\mathrm{c}} = 0.05\ \mathrm{s}^{-1}$) from raw data. The diffusion constant (D) is expressed as $D = 2\pi f_c d^2$, however, we evaluated the D by the least-squares fitting of the CIS, not from f_c. The D of NCdF94, NMnF84, and NCoF88 were $7.7\times10^{-10}\ \mathrm{cm}^2/\mathrm{s}$, $2.3\times10^{-10}\ \mathrm{cm}^2/\mathrm{s}$, and $0.6\times10^{-10}\ \mathrm{cm}^2/\mathrm{s}$, respectively. Similarly, we evaluated f_c of LCdF94 ($f_{\mathrm{c}} = 1.16\ \mathrm{s}^{-1}$), LMnF84 ($f_{\mathrm{c}} = 0.19\ \mathrm{s}^{-1}$) and the D of LCdF94 ($D = 3.5\times10^{-9}\ \mathrm{cm}^2/\mathrm{s}$), LMnF84 ($D = 4.6\times10^{-10}\ \mathrm{cm}^2/\mathrm{s}$).

3.1.3 Temperature dependence of complex impedance spectra

In order to investigate temperature (T) dependence of Na^+/ Li^+ diffusion constant (D), we measured the T-dependence of the complex impedance spectra (CIS). Figure 3.4 shows the T-dependence of CIS of (a) NCdF94, (b) NMnF84, and (c) NCoF88 films.

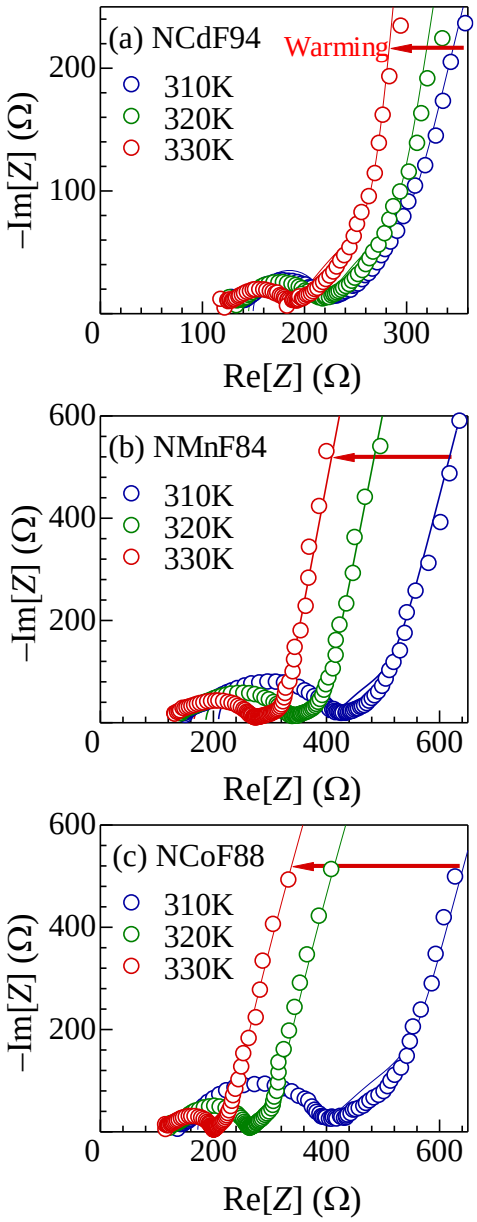

Figure 3.4 Temperature dependence of complex impedance spectra, (a) NCdF94, (b) NMnF84, and (c) NCoF88 films at various temperatures. Solid curves are results of the least squares fittings with the Randles equivalent circuit model. Data were cited and modified from Ref. [28].

The diameter of semicircle steeply decreases with increase in T, indicating a steep decrease in R_{ct}. The R_{ct} of NCdF94 was 69 Ω, 63 Ω, and 46 Ω at 310 K, 320 K, and 330 K, respectively. The R_{ct} of NMnF84 was 188 Ω, 139 Ω, and 102 Ω at 310 K, 320 K, and 330 K, respectively. The R_{ct} of NCoF88 was 209 Ω, 107 Ω, and 64 Ω at 310 K, 320 K, and 330 K, respectively.

Figure 3.5 shows the T-dependence of CIS of (a) LCdF94 and (b) LMnF84 films. In LMnF84 film, the diameter of semicircle steeply decreases with increase in T. The evaluation of R_{ct}, however, was difficult due to the semicircle were squashed.

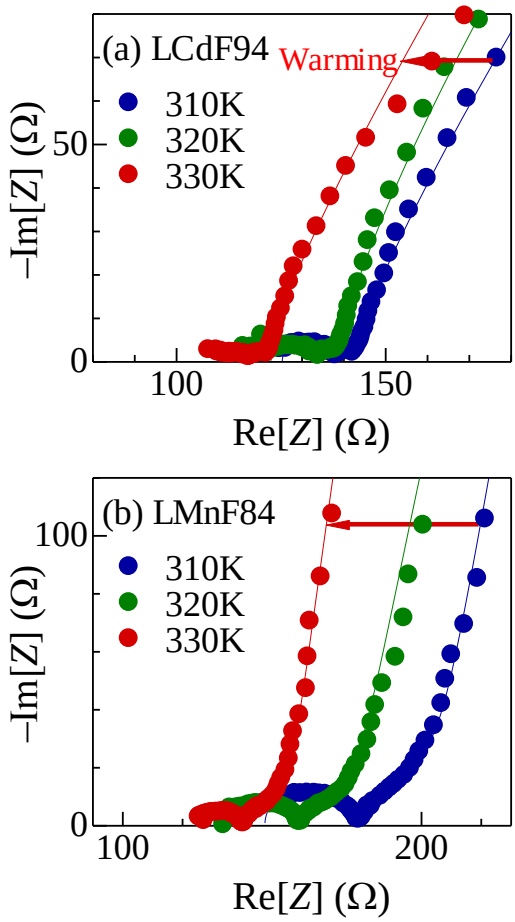

Figure 3.5 Temperature dependence of complex impedance spectra, (a) LCdF94 and (b) LMnF84 films at various temperatures. Solid curves are results of the least squares fittings with the Randles equivalent circuit model. Data were cited and modified from Ref. [28].

3.1.4 Activation energy of D

In order to determine the activation energy (E_a^D) of D, we plotted the temperature dependence of D. Figure 3.6 shows Arrhenius plot of D of (a) NCdF94, NMnF84, and NCoF88 films, (b) LCdF94 and LMnF84 films. Broken straight lines are results of least-squares fittings. As indicated by least-squares fitted lines, we found that D exponentially increases with decrease in T^{-1}. Thus, D obeys the thermal-activation law as follows:

$$D \propto \exp\left(-\frac{E_a^D}{k_B T}\right)$$

The magnitude of E_a^D were calculated from the slope of the fitted lines.

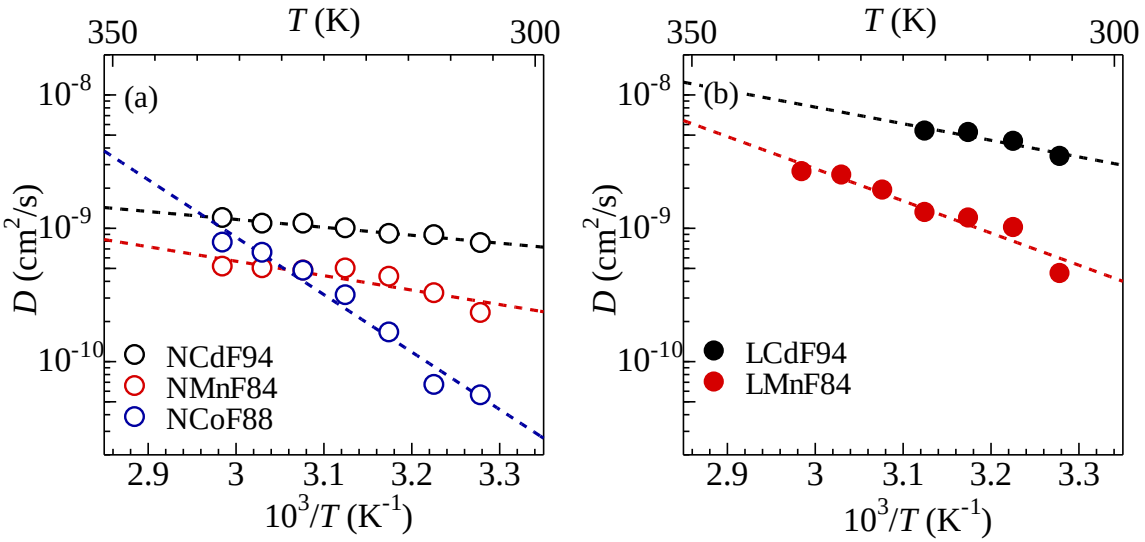

Figure 3.6 Arrhenius plot of D of (a) NCdF94, NMnF84, and NCoF88 films, (b) LCdF94 and LMnF84 films. Broken straight lines are results of least-squares fittings. Data were cited and modified from Ref. [28].

We listed D of NCdF94 (LCdF94), NMnF84 (LMnF84), and NCoF88 films against various temperatures in Table 4.

Table 4: The D of NCdF94 (LCdF94), NMnF84 (LMnF84), and NCoF88 films against various temperatures.

Temperature (K)	D of NCdF94 (cm^2/s)	D of NMnF84 (cm^2/s)	D of NCoF88 (cm^2/s)
305K	7.7×10^{-10}	2.3×10^{-10}	0.6×10^{-10}
310K	8.9×10^{-10}	3.3×10^{-10}	0.7×10^{-10}
315K	9.1×10^{-10}	4.3×10^{-10}	1.7×10^{-10}
320K	9.9×10^{-10}	4.9×10^{-10}	3.1×10^{-10}
325K	1.1×10^{-9}	4.8×10^{-10}	4.8×10^{-10}
330K	1.1×10^{-9}	5.0×10^{-10}	6.5×10^{-10}
335K	1.2×10^{-9}	5.1×10^{-10}	7.8×10^{-10}

Temperature (K)	D of LCdF94 (cm^2/s)	D of LMnF84 (cm^2/s)
305K	3.5×10^{-9}	4.6×10^{-10}
310K	4.5×10^{-9}	1.0×10^{-9}
315K	5.2×10^{-9}	1.2×10^{-9}
320K	5.3×10^{-9}	1.3×10^{-9}
325K	--------	1.9×10^{-9}
330K	--------	2.5×10^{-9}
335K	--------	2.7×10^{-9}

In order to determine the activation energy ($E_a^{R_{ct}}$) of R_{ct}, we plotted the temperature dependence of R_{ct}. Figure 3.7 shows Arrhenius plot of R_{ct} of NCdF94, NMnF84, and NCoF88 films. Broken straight lines are results of least-squares fittings. As indicated by least-squares fitted lines, we found that R_{ct} exponentially decreases with decrease in T^{-1}. Thus, R_{ct} obeys the thermal-activation law as follows:

$$R_{ct} \propto \exp\left(\frac{E_a^{R_{ct}}}{k_B T}\right)$$

The magnitude of $E_a^{R_{ct}}$ were calculated from the slope of the fitted lines.

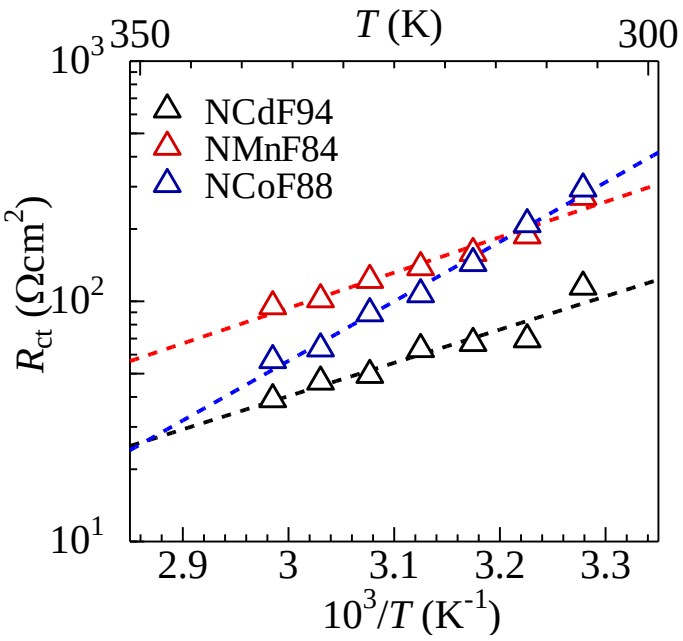

Figure 3.7 Arrhenius plot of R_{ct} of NCdF94, NMnF84, and NCoF88 films. Broken straight lines are results of least-squares fittings.

We listed R_{ct} of NCdF94, NMnF84, and NCoF88 films against various temperatures in Table 5.

Table 5: The R_{ct} of NCdF94, NMnF84, and NCoF88 films against various temperatures.

Temperature (K)	R_{ct} of NCdF94 (Ω)	R_{ct} of NMnF84 (Ω)	R_{ct} of NCoF88 (Ω)
305K	114	271	295
310K	69	188	209
315K	67	159	144
320K	63	139	107
325K	49	123	89
330K	46	102	64
335K	39	95	57

3.2 Discussion

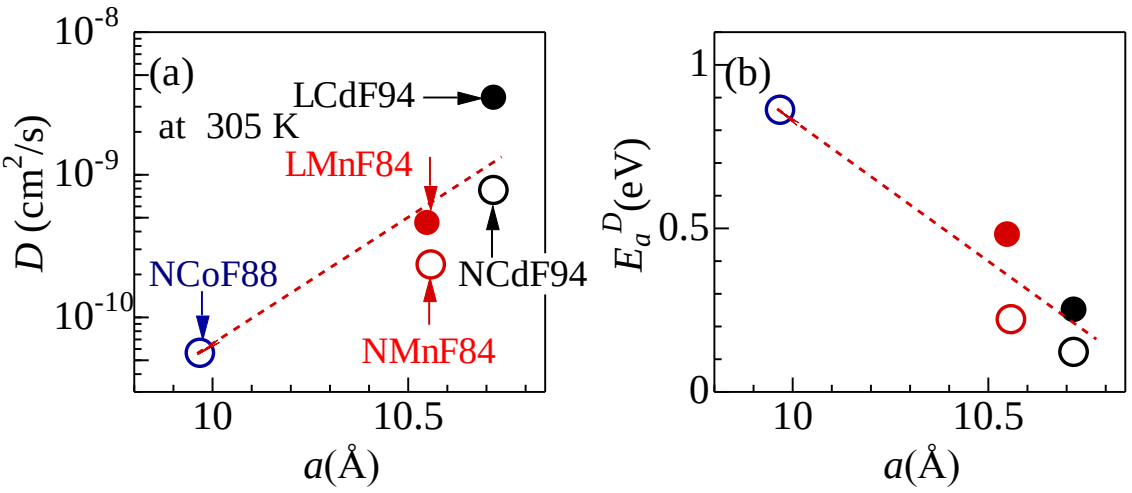

Figure 3.8 (a) Diffusion constant D and (b) activation energy E_a^D in NCdF94 (LCdF94), NMnF84 (LMnF84), and NCoF88 films against lattice constant a. Red broken straight lines are guided to the eye. Data were cited and modified from Ref. [28].

Figure 3.8 shows (a) diffusion constant (D) and (b) activation energy (E_a^D) in NCdF94 (LCdF94), NMNF84 (LMnF84), NCoF88 films against lattice constant a. The magnitudes of a were evaluated with use of the x dependence of a reported in literature [22-25,27]. For NCdF94, we used the structural data of the Li^+ substituted LCdF94. In Figure 3.8 (a), we found that the D of Na^+ steeply increases with increase in a: $D = 0.6 \times 10^{-10}$, 2.3×10^{-10}, 7.7×10^{-10} cm^2/s, at $a =$ 9.97 Å (NCoF88), 10.56 Å (NMnF84), and 10.70 Å (NCdF94), respectively. We further found that the D of Li^+ is much higher than D of Na^+ in Mn and Cd compounds. In Figure 3.8 (b), we found that E_a^D steeply decreases with increase in a: $E_a^D = 0.86$, 0.22, 0.12 eV at $a = 9.97$ Å (NCoF88), 10.56 Å (NMnF84), and 10.70 Å (NCdF94), respectively. Similarly, E_a^D steeply decreases with increase in a: $E_a^D = 0.48$, 0.25 eV at $a = 10.56$ Å (LMnF84) and $a = 10.70$ Å (LCdF94), respectively.

Y. Moritomo, and H. Tanaka performed *ab initio* total energy calculation in $A_xM_A[Fe(CN)_6]_yzH_2O$ (A = Li, Na, K, Rb, and Cs; M_A = Co, Ni, Mn, and Cd) and reported the heights of the potential barrier (ΔE) against the alkali cation position [20]. The calculated ΔE of Cs^+, Rb^+, and K^+ at the window position decrease with increase in a; ΔE = 2.3 (Cs^+), 1.2 (Rb^+), and 0.6 (K^+) eV/cation in $A_xCo[Fe(CN)_6]_y$ (a = 9.3440 Å), ΔE = 1.4 (Cs^+), 0.7 (Rb^+), and 0.2 (K^+) eV/cation in $A_xMn[Fe(CN)_6]_y$ (a = 10.5561 Å). This trend is in agreement with the experimental trend. The activation energy corresponds to the barrier height of the ion potential curve along the ion migration path. Figure 3.9 shows the schematic illustration of potential barrier vs. framework size for the Na^+ diffusion. With increase in the framework size, the height of the potential barrier decreases. A similar scenario is possible for the Li^+ diffusion, even though details of the Li^+ diffusion path is still unknown.

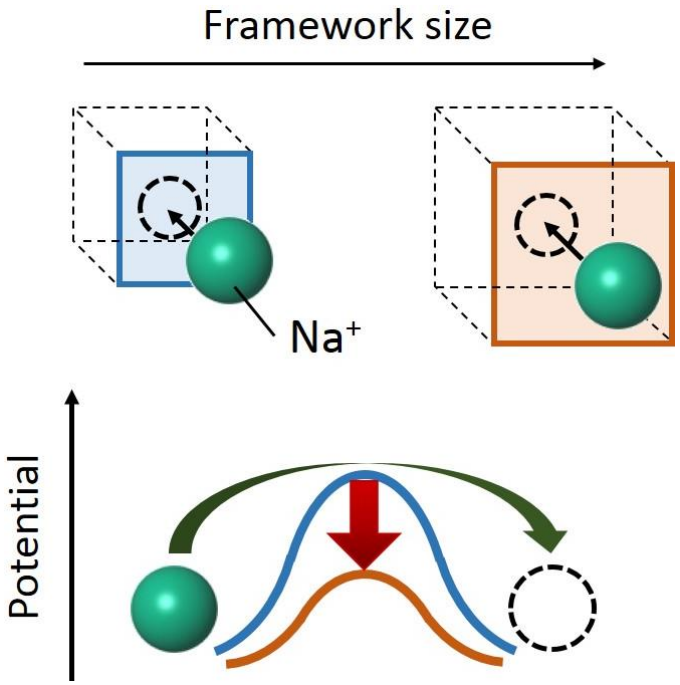

Figure 3.9 Schematic illustration of potential barrier vs. framework size for the Na^+ diffusion.

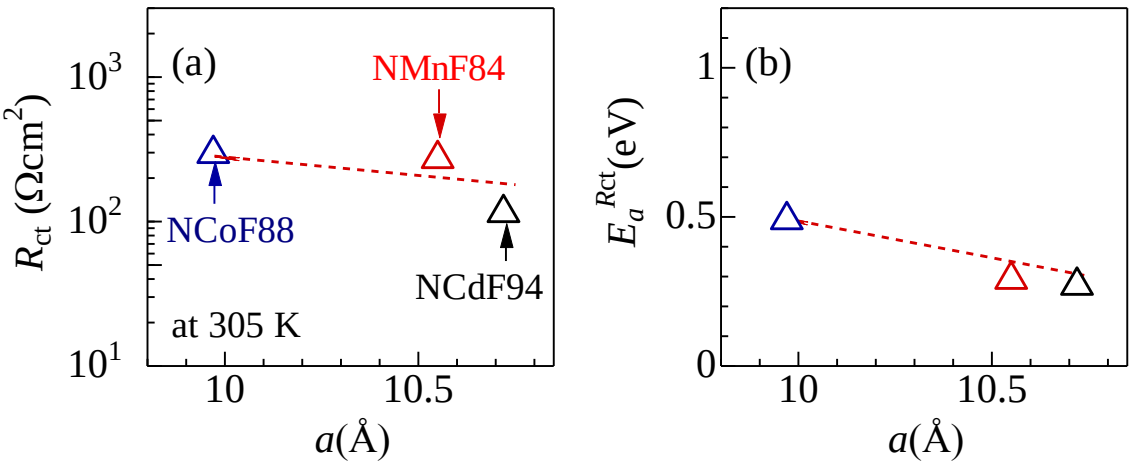

Figure 3.10 (a) Ionic charge-transfer resistance R_{ct} and (b) activation energy $E_a^{R_{ct}}$ in NCdF94, NMnF84, and NCoF88 films against lattice constant a. Red broken straight lines are guided to the eye.

Figure 3.10 shows (a) ionic charge-transfer resistance R_{ct}, and (b) activation energy $E_a^{R_{ct}}$ in NCdF94, NMnF84, and NCoF88 films against lattice constant a. The magnitude of R_{ct} is 295, 271, 114 Ω at a = 9.97 Å (NCoF88), 10.56 Å (NMnF84), and 10.70 Å (NCdF94), respectively. As shown in Figure 3.10 (b), the magnitude of $E_a^{R_{ct}}$ decrease gradually with increase in a : $E_a^{R_{ct}}$ = 0.49, 0.29, 0.27 eV at a = 9.97 Å (NCoF88), 10.56 Å (NMnF84), and 10.70 Å (NCdF94), respectively.

In general, the ionic charge-transfer process consist of the two processes, (i) the undressing process of the coordinated solvent in electrolyte and (ii) the intercalation of undressed ions at the electrolyte / active material interface. The potential barrier of the latter process is the same as that of the ion diffusion process. The magnitude of E_a^D and $E_a^{R_{ct}}$, however, does not necessarily the same because the ion diffusion environment is different between solid-to-solid diffusion and liquid-to-solid diffusion. We ascribed the rather decrease of $E_a^{R_{ct}}$ to the solvent effect.

3.3 Summary

In summary, we systematically determined the diffusion constant D and activation energy E_a against lattice constant a in thin films of Prussian blue analogues. We found that magnitude of D (E_a) increases (decreases) with increase in a. We ascribed the decrease of E_a to the increase of framework size.

4 Na^+ / Li^+ diffusion constant (D) vs. ion concentration x

4.1 Results

4.1.1 Discharge curve of the films

In order to prepare the films controlled ion concentration x, we performed charge / discharge measurement. Figure 4.1 shows discharge curves of (a) NMnF84 and (b) LMnF84 films. In NMnF84, the film and Na metal were used as the cathode and anode, and the electrolyte was ethylene carbonate / diethyl carbonate (EC / DEC) containing 1 mol/L $NaClO_4$. In LMnF84, the film and Li metal were used as the cathode and anode, and the electrolyte was ethylene carbonate / diethyl carbonate (EC / DEC) containing 1 mol/L $LiClO_4$.

In NMnF84, the discharge curve exhibits two plateau (I) and (II) measured at 0.5 C (see Figure 4.1 (a)). The observed discharge capacity (= 111 mAh/g) of NMnF84 was close to the ideal capacity (= 112 mAh/g) for the Na^+ intercalation from $x = 0.0$ to 1.36. In LMnF84, the discharge curve exhibits two plateau (I) and (II) measured at 0.5 C (see Figure 4.1 (b)).The observed discharge capacity (= 106 mAh/g) of LMnF84 was close to the ideal capacity (= 119 mAh/g) for the Li^+ intercalation from x = 0.0 to 1.36.

The valence states of transition metal were determined by the X-ray absorption spectroscopy (XAS) measurement around the Mn and Fe K-edges. In plateau (I) of NMnF84 and LMnF84, Mn K-edge spectra shows a clearly change with increase in x while Fe K-edge spectra does not shift. In contrast, Fe K-edge spectra shows a slight shift while Mn K-edge spectra does not change in plateau (II) [22,31]. Thus, plateaus (I) and (II) of NMnF84 and LMnF84 can be ascribed to the reduction of Mn and Fe, respectively. We listed discharge voltage (V) vs Na / Li metal, electronic configuration, and redox site of the respective plateaus (see Table 2 and Table 3).

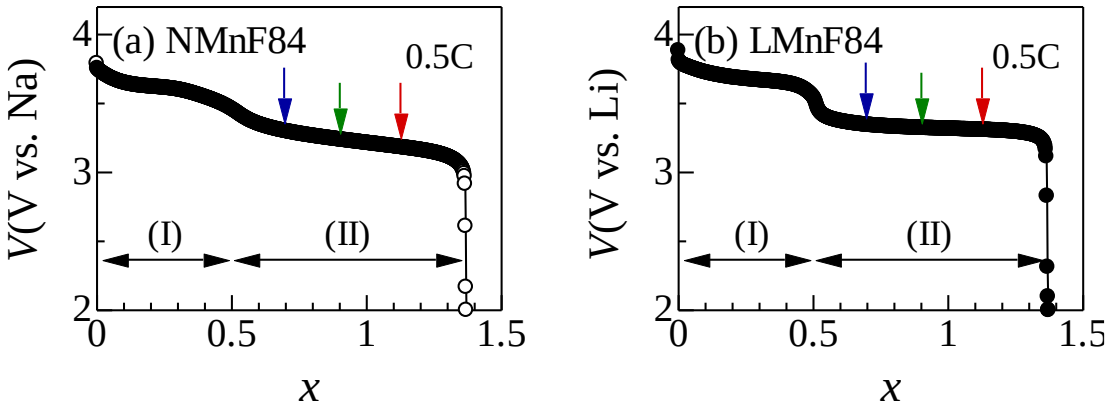

Figure 4.1 Discharge curves of (a) NMnF84 and (b) LMnF84 films. The redox of NMnF84 and LMnF84 in plateau (I), (II) are Mn and Fe, respectively. Arrows in the figure indicate the positions where CIS were measured.

Here, we assumed the ideal redox reactions of (a) NMnF84 and (b) LMnF84 in plateau (I), (II).

(a) Redox reactions of NMnF84

Plateau (I)

$1.36Na^{+} + Mn^{3+}_{0.52}Mn^{2+}_{0.48}[Fe^{3+}(CN)_6]_{0.84} \rightarrow 0.84Na^{+} + Na_{0.52}Mn^{2+}[Fe^{3+}(CN)_6]_{0.84}$

Plateau (II)

$0.84Na^{+} + Na_{0.52}Mn^{2+}[Fe^{3+}(CN)_6]_{0.84} \rightarrow Na_{1.36}Mn^{2+}[Fe^{2+}(CN)_6]_{0.84}$

(b) Redox reactions of LMnF84

Plateau (I)

$1.36Li^{+} + Mn^{3+}_{0.52}Mn^{2+}_{0.48}[Fe^{3+}(CN)_6]_{0.84} \rightarrow 0.84Li^{+} + Li_{0.52}Mn^{2+}[Fe^{3+}(CN)_6]_{0.84}$

Plateau (II)

$0.84Li^{+} + Li_{0.52}Mn^{2+}[Fe^{3+}(CN)_6]_{0.84} \rightarrow Li_{1.36}Mn^{2+}[Fe^{2+}(CN)_6]_{0.84}$

4.1.2 Complex impedance spectra

In order to investigate Na^+ / Li^+ diffusion constant (D), we measured complex impedance spectra (CIS) vs. ion concentration x. Figure 4.2 shows the CIS of (a) NMnF84 ($x = 0.7$) against Na metal at 305K, (b) LMnF84 ($x = 0.7$) against Li metal at 305K. The frequency range was from 200 kHz to 5 mHz. Arrows in the figure indicate the frequencies. Broken straight lines are guided to the eye. Solid curves are results of the least-squares fittings with the Randles equivalent circuit model.

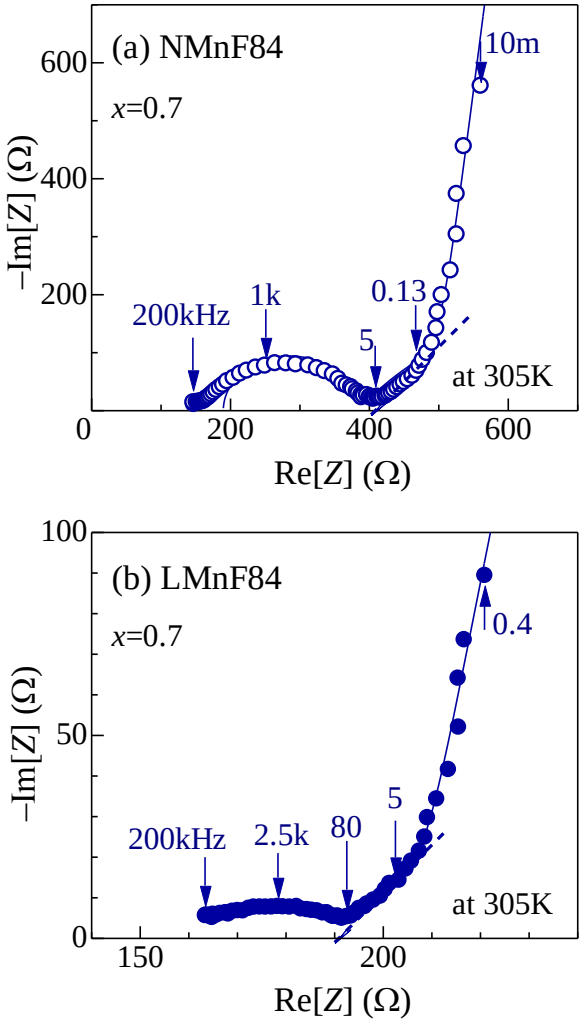

Figure 4.2 Complex impedance spectra of (a) NMnF84 ($x = 0.7$) and (b) LMnF84 ($x = 0.7$). The frequency range was from 200 kHz to 5 mHz. Arrows in the figure indicate the frequencies. Broken straight lines are guided to the eye. Solid curves are results of the least squares fittings with the Randles equivalent circuit model. Data were cited and modified from Ref. [31].

In the high frequency region, the spectra shows semicircle due to ionic charge-transfer resistance (R_{ct}) and electric double-layer capacitance (C_{dl}). In NMnF84 at $x = 0.7$, R_{ct} and C_{dl} were 188 Ω and 1.4×10^{-6} F, respectively. In LMnF84, the evaluations of R_{ct} and C_{dl} were difficult because of the squashed semicircles of CIS. With the decrease in the frequency f, the CIS form straight lines with the angle of $\pi/4$ against the real axis (broken straight line). With further decrease in the frequency f, the CIS deviate from the broken line. We evaluated the critical frequency f_c of NMnF84 ($f_{\mathrm{c}} = 0.13\ \mathrm{s}^{-1}$) and LMnF84 ($f_{\mathrm{c}} = 5.0\ \mathrm{s}^{-1}$) from raw data. The D of NMnF84 and LMnF84 were 2.8×10^{-10} cm^2/s and 1.1×10^{-8} cm^2/s, respectively.

4.1.3 Temperature dependence of complex impedance spectra

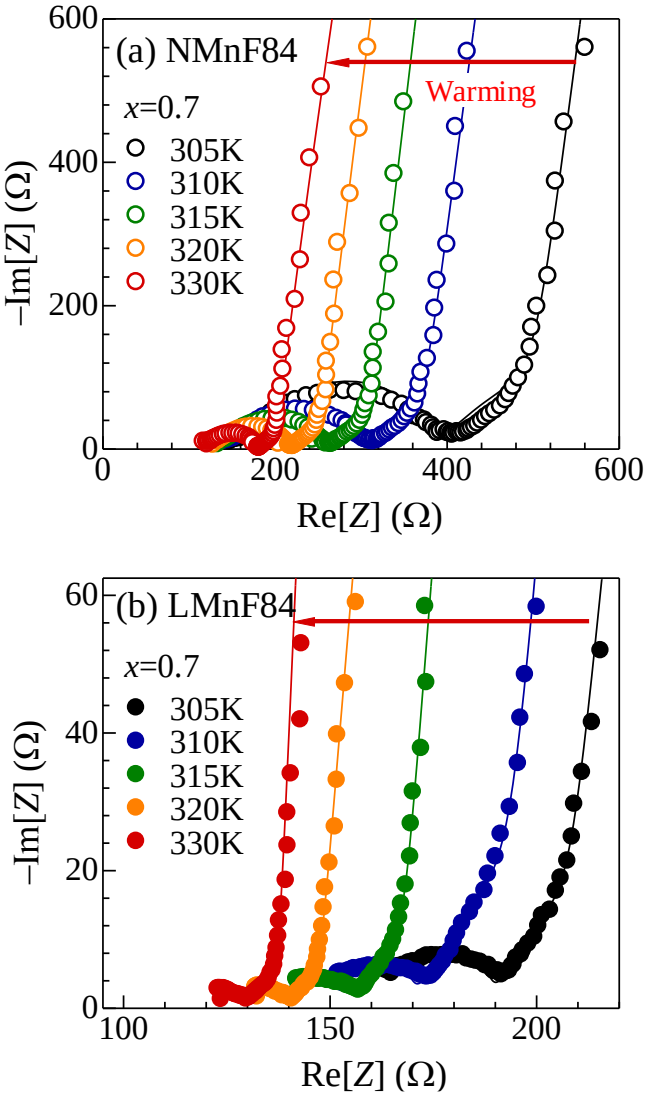

Figure 4.3 Temperature (T) dependence of the CIS of (a) NMnF84 ($x = 0.7$), (b) LMnF84 ($x = 0.7$). Solid curves are results of the least squares fittings with the Randles equivalent circuit model. Data were cited and modified from Ref. [31].

Figure 4.3 shows temperature (T) dependence of the CIS of (a) NMnF84 ($x = 0.7$) and (b) LMnF84 ($x = 0.7$). In NMnF84, the diameter of semicircle steeply decreases with increasing T, indicating a steep decrease in R_{ct}. In NMnF84 at $x = 0.7$, R_{ct} decreased 188 Ω (at 305 K) to 50 Ω (at 330 K). In LMnF84, the evaluation of R_{ct} was difficult because of the semicircle of CIS cannot be fitted by Randles equivalent circuit model.

4.1.4 Activation energy of D and R_{ct}

In order to determine the activation energy ($E_a^{Na/Li}$) of D, we plotted the temperature dependence of D. Figure 4.4 shows Arrhenius plot of D of (a) NMnF84 and (b) LMnF84 film. Broken straight lines are results of least-squares fittings. As indicated by least-squares fitted lines, we found that D exponentially increases with decreasing T^{-1}. Thus, D obeys the thermal-activation law as follows:

$$D \propto \exp\left(-\frac{E_a^{Na/Li}}{k_B T}\right)$$

The magnitude of $E_a^{Na/Li}$ were calculated from the slope of the fitted lines.

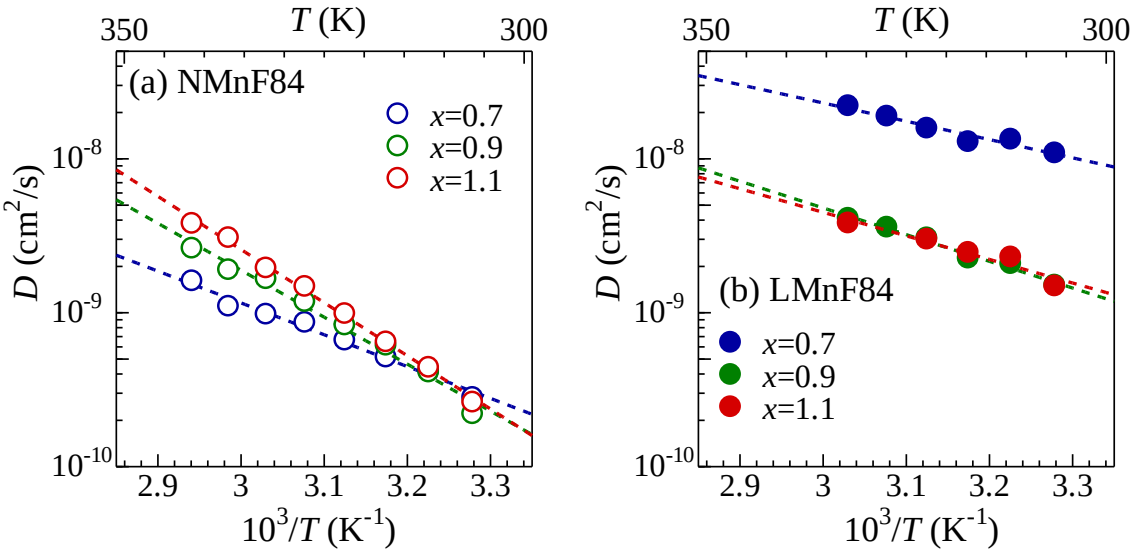

Figure 4.4 Arrhenius plot of D of (a) NMnF84, and (b) LMnF84 film. Broken straight lines are results of least-squares fittings. Data were cited and modified from Ref. [31].

We listed the D of NMnF84 and LMnF84 films against various temperatures in Table 6.

Table 6: The D of NMnF84 and LMnF84 films against various temperatures.

NMnF84	D $(x = 0.7)$ (cm^2/s)	D $(x = 0.9)$ (cm^2/s)	D $(x = 1.1)$ (cm^2/s)
305 K	2.8×10^{-10}	2.2×10^{-10}	2.6×10^{-10}
310 K	4.2×10^{-10}	4.1×10^{-10}	4.4×10^{-10}
315 K	5.1×10^{-10}	6.1×10^{-10}	6.5×10^{-10}
320 K	6.6×10^{-10}	8.3×10^{-10}	9.9×10^{-10}
325 K	8.6×10^{-10}	1.2×10^{-9}	1.5×10^{-9}
330 K	9.8×10^{-10}	1.7×10^{-9}	1.9×10^{-9}
335 K	1.1×10^{-9}	1.9×10^{-9}	3.1×10^{-9}
340 K	1.6×10^{-9}	2.6×10^{-9}	3.8×10^{-9}

LMnF84	D $(x = 0.7)$ (cm^2/s)	D $(x = 0.9)$ (cm^2/s)	D $(x = 1.1)$ (cm^2/s)
305 K	1.1×10^{-8}	1.5×10^{-9}	1.5×10^{-9}
310 K	1.3×10^{-8}	2.1×10^{-9}	2.3×10^{-9}
315 K	1.3×10^{-8}	2.3×10^{-9}	2.5×10^{-9}
320 K	1.6×10^{-8}	3.1×10^{-9}	3.0×10^{-9}
325 K	1.9×10^{-8}	3.6×10^{-9}	--------
330 K	2.2×10^{-8}	4.1×10^{-9}	3.8×10^{-9}

In order to determine the activation energy (E_a^{Na}) of R_{ct}, we plotted the temperature dependence of R_{ct}. Figure 4.5 shows Arrhenius plot of R_{ct} of NMnF84 film. Broken straight lines are results of least-squares fittings. As indicated by least-squares fitted lines, we found that R_{ct} exponentially decreases with decreasing T^{-1}. Thus, R_{ct} obeys the thermal-activation law as follows:

$$R_{\mathrm{ct}} \propto \exp\left(\frac{E_a^{\mathrm{Na}}}{k_B T}\right)$$

The magnitude of E_a^{Na} were calculated from the slope of the fitted lines.

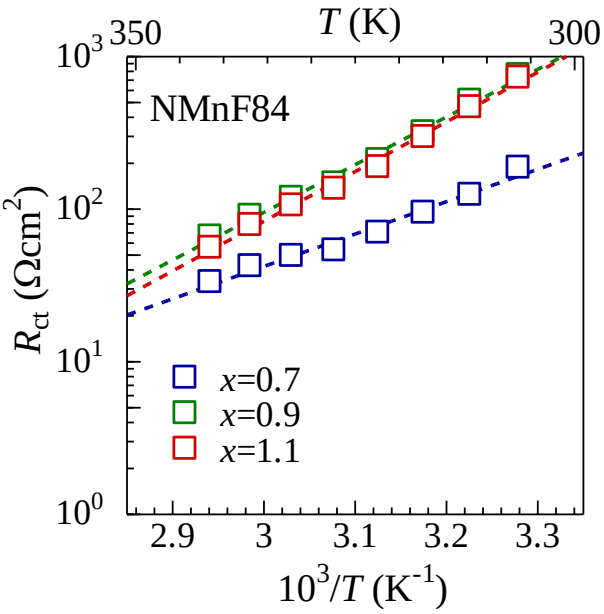

Figure 4.5 Arrhenius plot of R_{ct} of NMnF84 film. Broken straight lines are results of least-squares fittings. Data were cited and modified from Ref. [31].

We listed the R_{ct} of NMnF84 and LMnF84 films against various temperatures in Table 7.

Table 7: The R_{ct} of NMnF84 and LMnF84 films against various temperatures.

NMnF84	R_{ct} $(x = 0.7)$ (Ω)	R_{ct} $(x = 0.9)$ (Ω)	R_{ct} $(x = 1.1)$ (Ω)
305 K	188	759	731
310 K	125	516	468
315 K	95	321	298
320 K	71	211	189
325 K	54	148	137
330 K	49	119	106
335 K	42	91	79
340 K	33	66	56

4.2 Discussion

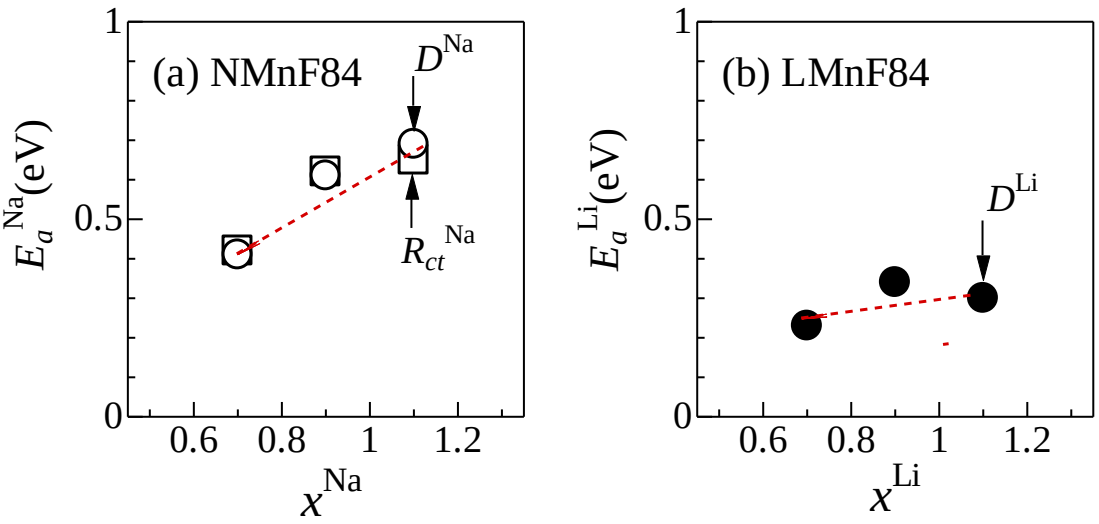

Figure 4.6 (a) Activation energies E_a^{Na} of D^{Na} (circles) and R_{ct}^{Na} (squares) in NMnF84 films against x^{Na}. (b) Activation energies E_a^{Li} of D^{Li} (circles) in LMnF84 films against x^{Li}. Red broken straight lines are guided to the eye. Data were cited and modified from Ref. [31].

Figure 4.6 shows (a) activation energies E_a^{Na} of D^{Na} (circles) and R_{ct}^{Na} (squares) in NMnF84 films against x^{Na}, (b) activation energies E_a^{Li} of D^{Li} (circles) in LMnF84 films against x^{Li}. In Figure 4.6 (a), we found that E_a^{Na} steeply increases from 0.41 eV at $x^{Na} = 0.7$ to 0.69 eV at $x^{Na} = 1.1$. In Figure 4.6 (b), increasing E_a^{Li} is suppressed in the LMnF84 film, $E_a^{Li} = 0.23$ eV at $x^{Li} = 0.7$ to 0.30 eV at $x^{Li} = 1.1$. We found that the E_a^{Na} of R_{ct}^{Na} in NMnF84 film is nearly the same as those of D^{Na}.

Let us discuss the origin of the steep increase in E_a^{Na} with x^{Na}. First, we consider the structural effect. T. Matsuda, *et al.* [23] reported the lattice constant a of the $Na_xMn[Fe(CN)_6]_{0.83}3.5H_2O$ (denoted as NMnF83) film against x^{Na}. In the bottom panel of Figure 4.7 (a), we replotted a of NMnF83. NMnF83 belongs to the face centered cubic structure in the entire x^{Na} region ($0.0 < x^{Na} < 1.32$). In the CIS investigated x^{Na} region ($0.7 < x^{Na} < 1.1$), a slightly decreases with x^{Na} from a =10.57 Å at x^{Na} =0.7 to a =10.55 Å at x^{Na} = 1.1. The compression of the host framework can explain the observed increase in E_a^{Na}, because the compression heightens the potential barrier between the neighboring Na sites.

This scenario, however, fails to explain the suppressed increase in E_a^{Li} with x^{Li}. In the bottom panel of Figure 4.7 (b), we replotted the lattice constant a of $Li_xMn[Fe(CN)_6]_{0.83}3.5H_2O$ (denoted as LMnF83) [22]. The LMnF83 belongs to the face centered cubic structure in the entire x^{Li} region ($0.0 < x^{Li} < 1.32$). In the CIS investigated x^{Li} region ($0.7 < x^{Li} < 1.1$), a significantly decreases with x^{Li} from a =10.53 Å at x^{Li} =0.7 to a =10.48 Å at x^{Na} =1.1. Such a compression of the host framework would cause a steeper increase in E_a^{Li}, however, which contradict with the observation.

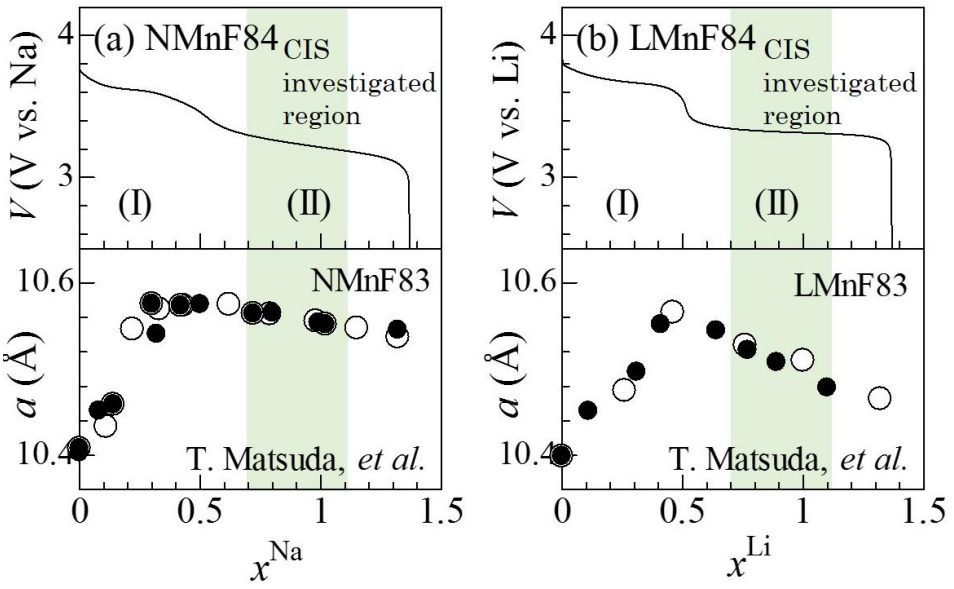

Figure 4.7 Upper panel: the discharge curve of (a) NMnF84 and (b) LMnF84 films. Bottom panel: the lattice constant a of (a) NMnF83 and (b) LMnF83 against $x^{Na/Li}$. Green square represents the CIS investigated region ($0.7 < x^{Na/Li} < 1.1$). Data were cited and modified from Ref. [22,23,31].

Another possible origin for the increase in E_a^{Na} is the occupancy effect of the ion sites. Here, let us define normalized ion concentration $x_{\mathrm{norm}}^{\mathrm{Na/Li}}$.

$$x_{\mathrm{norm}}^{\mathrm{Na/Li}} \equiv x^{\mathrm{Na/Li}} / n^{\mathrm{Na/Li}}$$

where $n^{\mathrm{Na/Li}}$ is the number of Na / Li sites per Mn site. Y. Moritomo, *et al.* measured X-ray powder diffraction pattern in NMnF83 and analyzed that Na^+ is located around the tetragonal site close to the central position [32,33]. The nano-cube can accommodate one Na^+ in maximum and hence n^{Na} =2. T. Matsuda, *et al.* [23] performed the Rietveld structural analysis of $Li_{0.9}Mn[Fe(CN)_6]_{0.83}3.5H_2O$. They found that the central region of nano-cube is occupied by crystal water (zeolite water). This report suggest that Li^+ is located at near the face of the nano-cube. The nano-cube can accommodate three Li^+ in maximum and hence n^{Li} =6. Figure 4.8 shows activation energies $E_a^{\mathrm{Na/Li}}$ vs. $x_{\mathrm{norm}}^{\mathrm{Na/Li}}$. This result suggest that $E_a^{\mathrm{Na/Li}}$ has a strong positive correlation with $x_{\mathrm{norm}}^{\mathrm{Na/Li}}$.

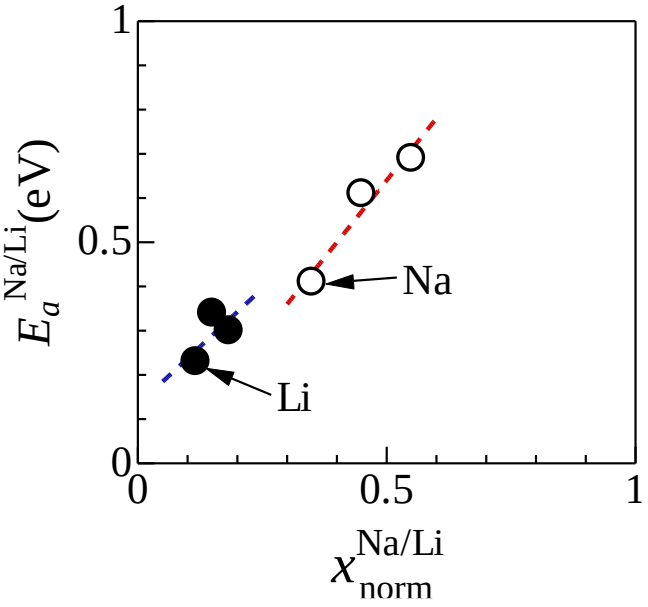

Figure 4.8 Activation energies $E_a^{\mathrm{Na/Li}}$ vs. normalized concentration $x_{\mathrm{norm}}^{\mathrm{Na/Li}}$.($= x^{\mathrm{Na/Li}} / n^{\mathrm{Na/Li}}$, where $x^{\mathrm{Na/Li}}$ is the Na^+ / Li^+ number per Mn site, and $n^{\mathrm{Na/Li}}$ is the number of Na / Li sites per Mn site)

Figure 4.9 shows the schematic illustrations of the Na^+ diffusion in (a) low-x and (b) high-x region. In the low-x region (Figure 4.9 (a)), Na^+ easily moves to the neighboring site. In the high-x region (Figure 4.9 (b)), however, the Na^+ diffusion is frequently blocked by the another Na^+ at the neighboring site. Consequently, the effective activation energy becomes higher in the high-x region.

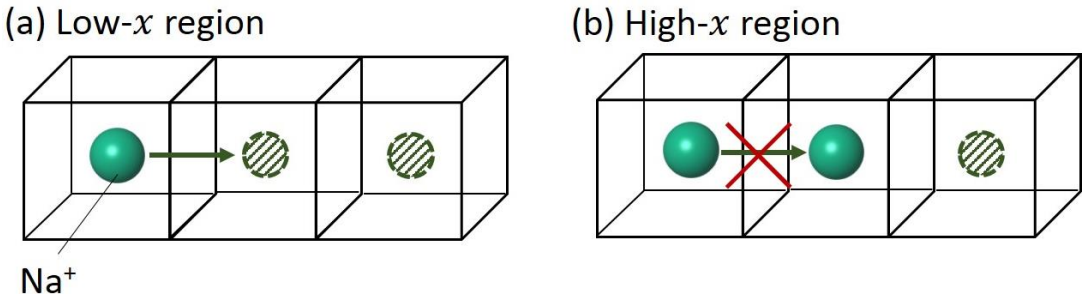

Figure 4.9 Schematic illustrations of the Na^+ diffusion in (a) low-x and (b) high-x region. Broken spheres represent vacant sites.

4.3 Summary

In summary, we systematically determined the diffusion constant $D^{\mathrm{Na/Li}}$ and activation energy $E_a^{\mathrm{Na/Li}}$ against $x^{\mathrm{Na/Li}}$ in $Na_xMn[Fe(CN)_6]_{0.84}3.4H_2O$ (NMnF84) and $Li_xMn[Fe(CN)_6]_{0.84}3.4H_2O$ (LMnF84). We observed the steep increase of E_a^{Na} against x^{Na} in NMnF84 film. In contrast, the increase of E_a^{Li} against x^{Li} were suppressed in LMnF84 film. We ascribed the increase of E_a^{Na} against x^{Na} to the small number of Na^+ site.

5 *In situ* microscopic observation in $Li_xCo[Fe(CN)_6]_{0.90}$

5.1 Results

5.1.1 Li^+ concentration x vs. visible absorption spectra

We observed the film color against Li^+ concentration x in a handmade beaker-type two-pole cell. Figure 5.1 shows (Upper panel) charge curve of LCoF90 (d = 1.5 μm) and (Lower panel) film color images against x. The film and Li metal were used as the cathode and anode, respectively. The electrolyte was ethylene carbonate / diethyl carbonate (EC / DEC) containing 1 mol/L $LiClO_4$.

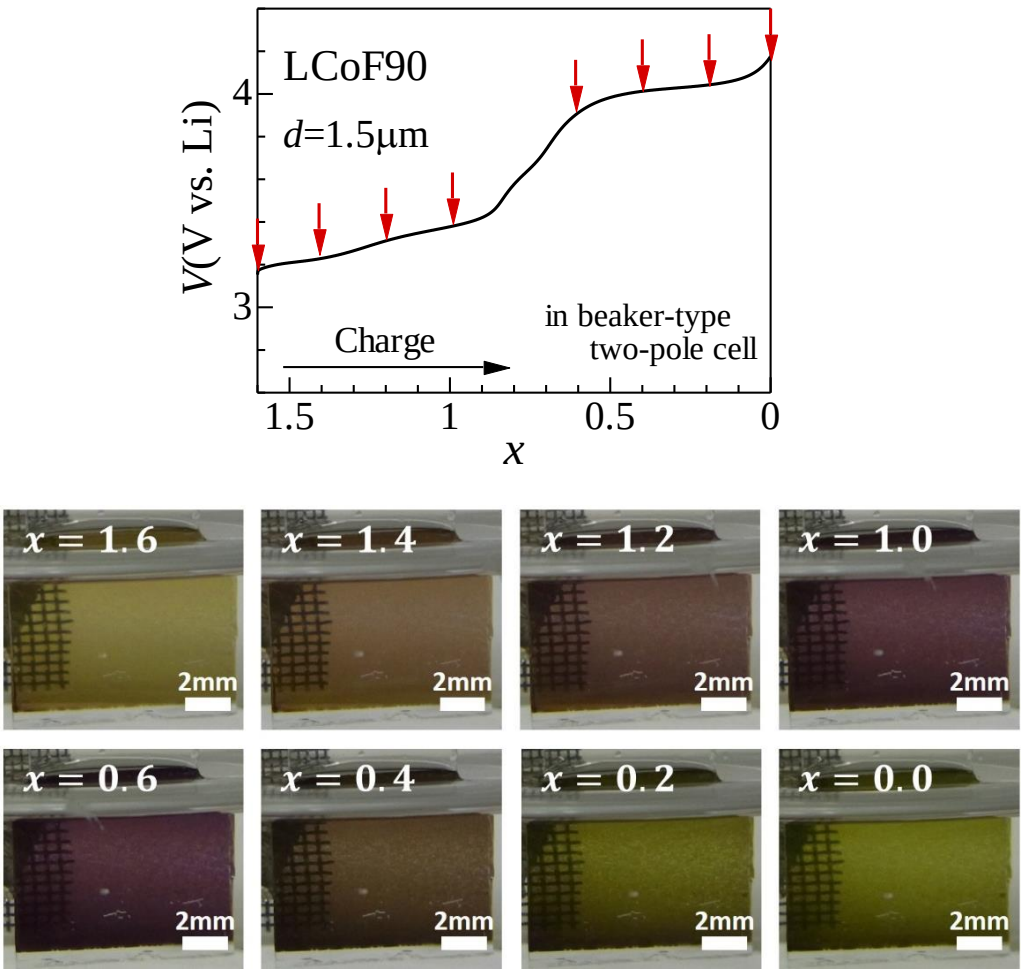

Figure 5.1 Upper panel: charge curve of LCoF90 film (d = 1.5 μm) against x. Lower panel: film color images at respective x, indicated red allows in the charge curve.

As shown in lower panel, the color of LCoF90 film shows transparent green at $x = 1.6$. With decrease in x, the film color changes from transparent green to transparent violet at around $x = 1.4$. With further decrease in x, the film color changes from transparent violet to transparent green at around $x = 0.6$. We confirmed the film color change of discharge process is reversible.

Figure 5.2 shows the visible absorption spectra of LCoF90 film ($d = 1.0$ μm) against x. The absorption band observed at around 380 nm and 540 nm are ascribed to the charge transfer from Fe^{2+} to the neighboring Co^{2+} and Fe^{2+} to the neighboring Co^{3+}, respectively [34]. The absorption band at around 540 nm increases significantly with decrease in x. Thus, the 540 nm band can be used as a sensitive monitor to observe the change of film color.

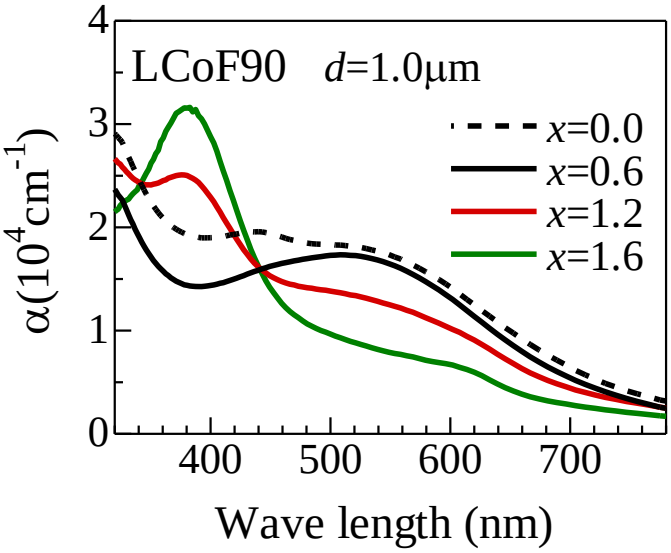

Figure 5.2 Visible absorption spectra of LCoF90 film ($d = 1.0$ μm) against x. The absorption observed around 380 nm and 540 nm are ascribed to the charge transfer from Fe^{2+} to the neighboring Co^{2+} and Fe^{2+} to the neighboring Co^{3+}, respectively [34]. Data were cited and modified from Ref. [35].

5.1.2 *In situ* microscopic observation (d = 1.5 μm)

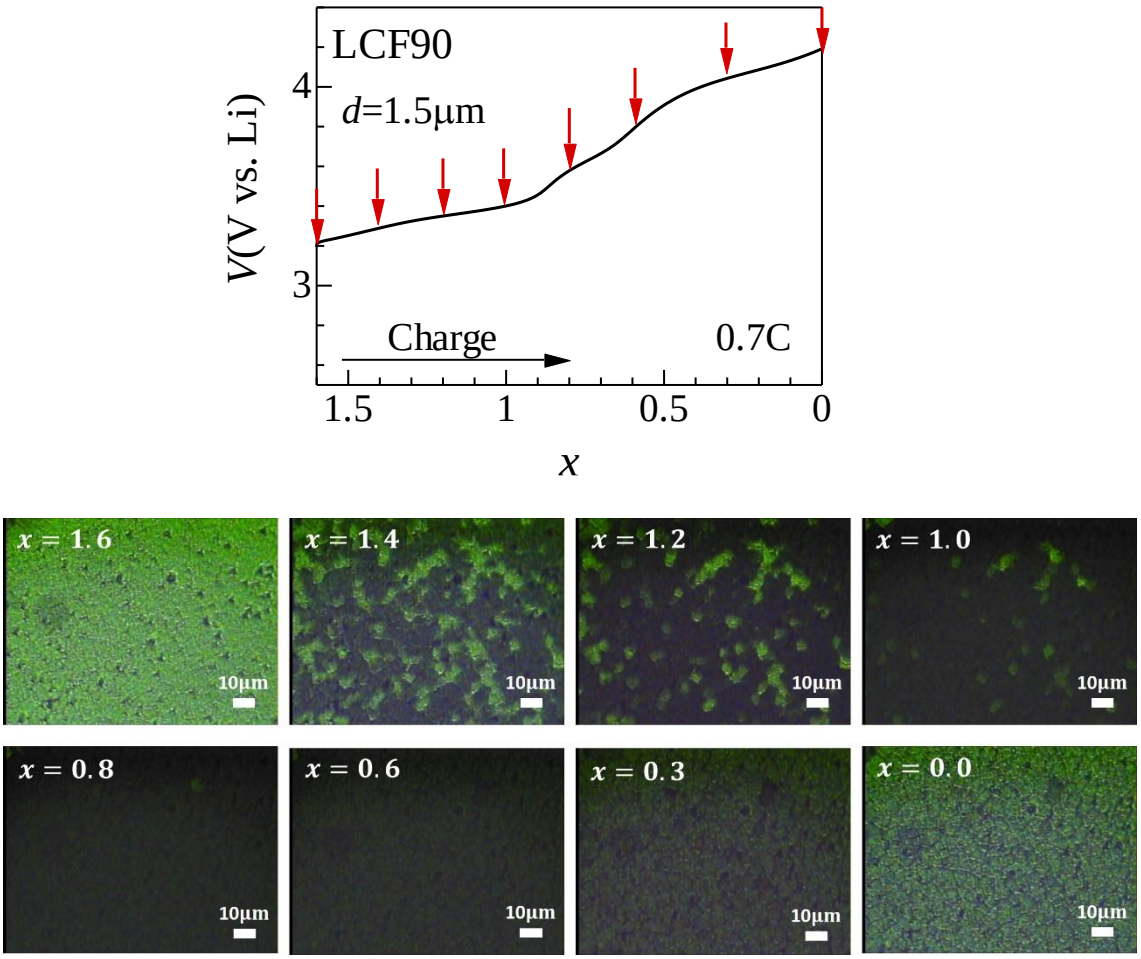

Figure 5.3 Upper panel: charge curve of LCoF90 film (d = 1.5 μm) against x. Lower panel: microscopic images at respective x, indicated red allows in the charge curve. Data were cited and modified from Ref. [35].

Figure 5.3 shows the charge curve of LCoF90 film (d = 1.5 μm) at 0.7 C against x, together with the microscopic images. In the late state ($0.0 < x < 0.6$) of the charge curve, a plateau at around 4.0 V is observed. This plateau is ascribed to the oxidation process of Fe^{2+} to Fe^{3+} [24].

At $x = 1.6$, the microscopic image is homogeneous green. In microscopic observation, we monitored images through a dichronic filter (DIF-50S-GRE: Sigma Kouki Co. Ltd.). The transmission range of the filter is 515 ~ 560 nm and hence the microscopic image is green. With decrease in x, the black region appear in the image at $x = 1.4$. The black region is the area where light cannot transmit the filter. With further decrease in x, the black region increases in area ($x = 1.0$, 1.2). Finally, the black region covers the entire image ($x = 0.8$, 0.6). Looking carefully at $x = 1.4$, 1.2, and 1.0 images, the size of the green region gradually shrinks without changing the green color. This means that no nucleation of micro-domain of black region occurs within the green region.

Here, we considered the chemical composition of green and black region. The visible absorption of 540 nm band is ascribed to the charge transfer from Fe^{2+} to the neighboring Co^{3+}. We considered that the proportion of Co^{3+} in black region is larger than that of the green region. The chemical composition of as-grown NCoF90 is $Na_{1.6}Co^{2+}[Fe^{2+}(CN)_6]_{0.90}$. Thus, the green region is considered the green phase ($Li_{1.6}Co^{2+}[Fe^{2+}(CN)_6]_{0.90}$). The ideal reactions of delithiation process is as follows; $Li_{1.6}Co^{2+}[Fe^{2+}CN)_6]_{0.90} \rightarrow Li^+ + Li_{0.6}Co^{3+}[Fe^{2+}(CN)_6]_{0.90}$. Then, the chemical composition of the black region is considered the black phase ($Li_{0.6}Co^{3+}[Fe^{2+}(CN)_6]_{0.90}$). Therefore, we observed the macroscopic phase separation (PS) in the thick film. The transformation from the green phase to black phase progresses at the phase boundary. In the late state ($0.0 < x < 0.6$), the images gradually becomes bright ($x = 0.3$, 0.0), because parts of Fe^{2+}, which is the final state of the optical transition, are oxidized to Fe^{3+}. We further investigated the PS dynamics at much higher rate (= 47 C) and found that the PS behavior is essentially the same as that at low rate (= 0.7 C). This observation indicates that the PS dynamics is very fast.

5.1.3 Lattice constant a of green and black region

We measured the synchrotron-radiation X-ray powder diffraction pattern at BL02B2 beamline of SPring-8 [36]. The film was torn off the ITO transparent electrode and was sealed in a 0.3mmϕ glass capillaries. The capillary was placed on a large Debye-Scherrer camera. The wavelength (= 0.49832 Å) of the X-ray was calibrated by the lattice constant of standard CeO_2 powders. The diffraction patterns were detected with an imaging plate manufactured by Fujifilm Corporation. The exposure time was 5 minutes. The diffraction pattern were analyzed by Rietveld method (RIETAN-FP [29]) with two face centered cubic ($Fm\underline{3}m$) phases. We omitted Li and ligand O in the analysis. Figure 5.4 shows the X-ray powder diffraction pattern of the LCoF90 film ($x = 1.2$). The lattice constants were evaluated $a =$ 10.18405 ± 0.00153 Å and 9.95259 ± 0.00160 Å. M. Takachi, *et. al.* [26] reported that the lattice constant of as-grown NCoF90 ($x = 1.6$) is 10.20 Å. Therefore, the lattice constant of green phase (a_G) and black phase (a_B) are ascribed to 10.18405 ± 0.00153 Å and 9.95259 ± 0.00160 Å, respectively.

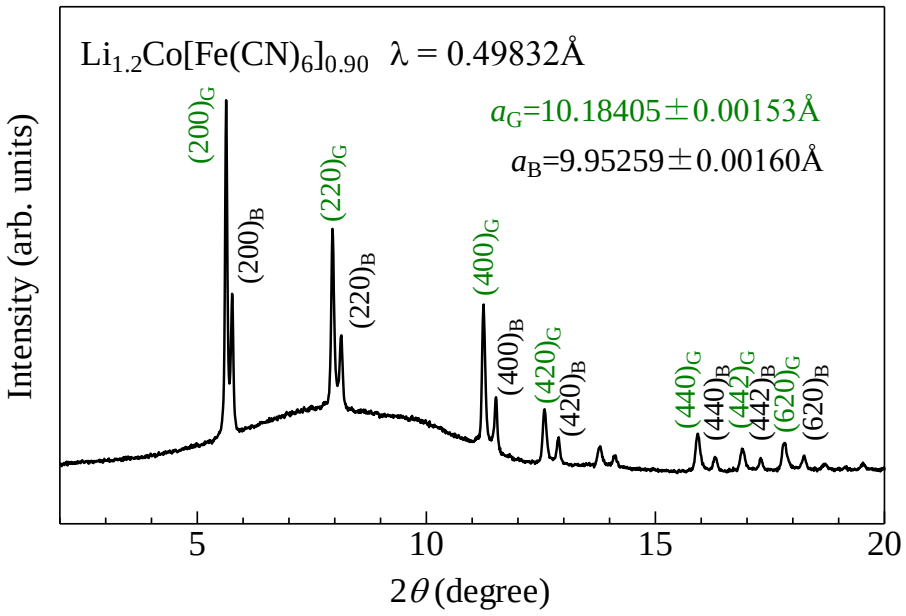

Figure 5.4 Synchrotron-radiation X-ray powder diffraction pattern of the LCoF90 ($x = 1.2$). The wavelength of the X-ray was 0.49832 Å. Data were cited and modified from Ref. [35].

Figure 5.5 shows the distributions of linear expansion ($\Delta L/L$) coefficient (a) green region, (b) black region, and (c) microscopic images at $x = 1.6$ and 1.4 in LCoF90 film ($d = 1.5$ μm). The ΔL values were represented by the subtraction of L ($x = 1.6$) from L' ($x = 1.4$) with use of spots at the gain boundaries. We evaluated $\Delta L/L = -0.013 \pm 0.012$ in the black region while $\Delta L/L = -0.004 \pm 0.013$ in the green region. Around 1% contraction in the black phase is consistent with the fact that the lattice constant (= 9.95 Å) in the black phase is shorter than that (= 10.2 Å) in the green phase.

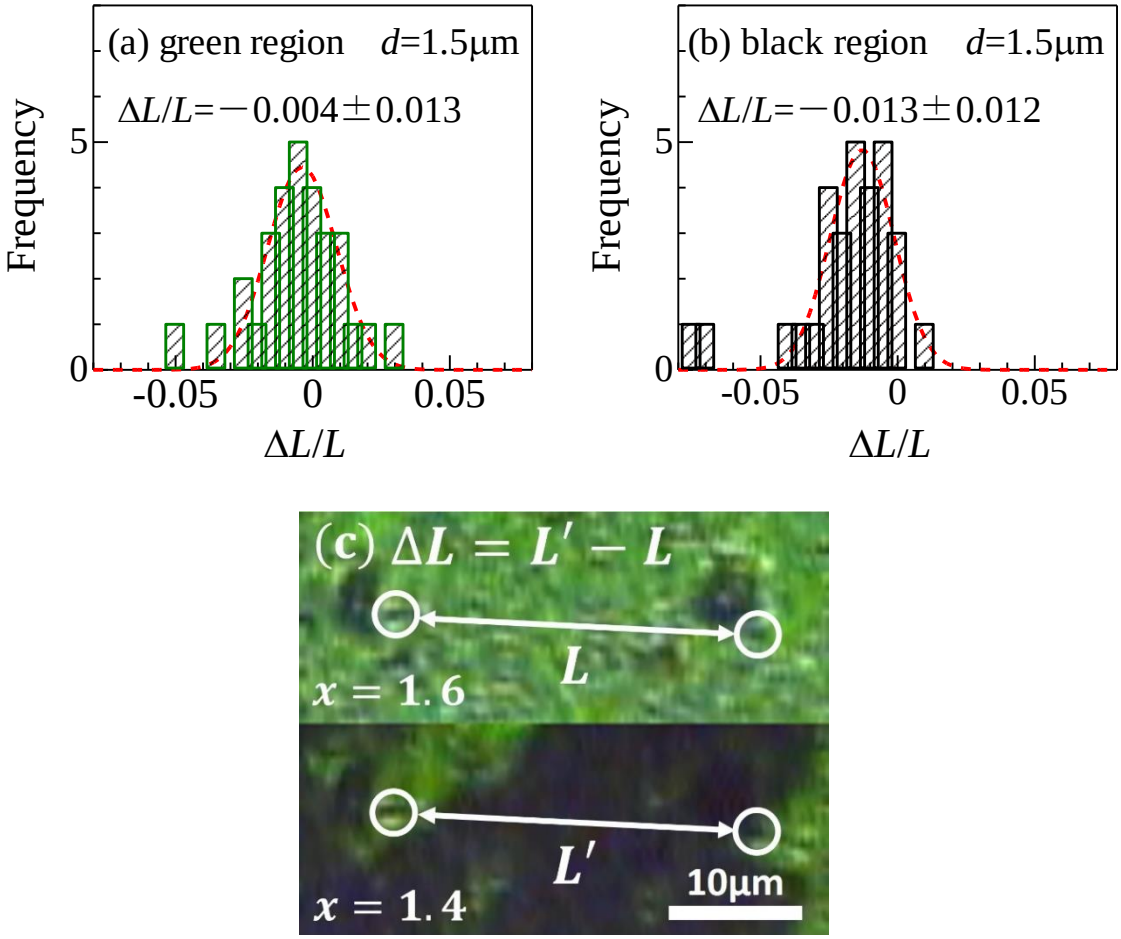

Figure 5.5 Distributions of linear expansion ($\Delta L/L$) coefficient (a) green region, (b) black region, and (c) the microscopic images at $x = 1.6$ and 1.4 in LCoF90 film ($d = 1.5$ μm). The ΔL values were represented by the substruction of L ($x = 1.6$) from L' ($x = 1.4$) with use of spots at the gain boundaries. The broken curves represent the results of Gauss fitting. Data were cited and modified from Ref. [35].

5.1.4 *In situ* microscopic observation ($d = 0.5$ μm)

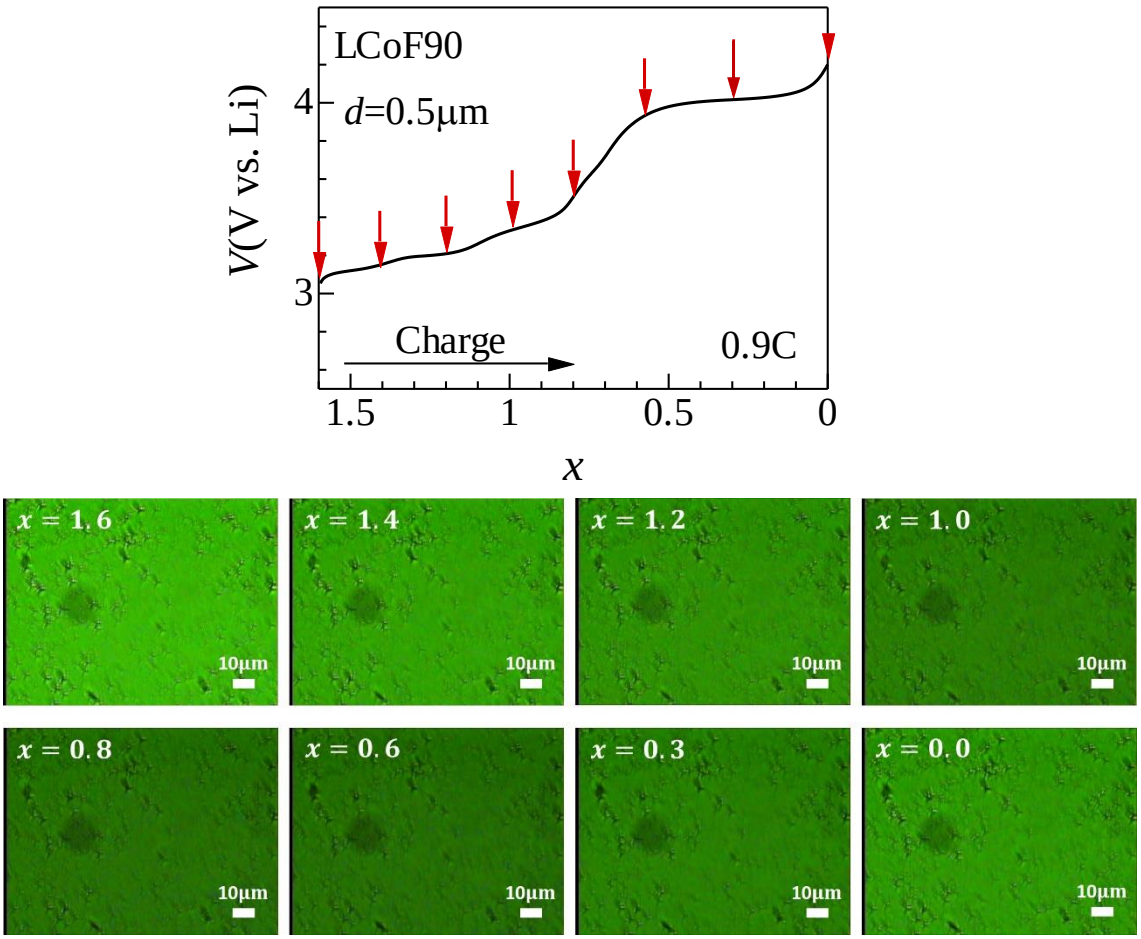

Figure 5.6 Upper panel: charge curve of LCoF90 film ($d = 0.5$ μm) against x. Lower panel: microscopic images at respective x, indicated red allows in the charge curve. Data were cited and modified from Ref. [35].

Figure 5.6 shows the charge curve of LCoF90 film ($d = 0.5$ μm) at 0.9 C against x, together with the microscopic images. We observed no trace of the macroscopic PS. The image becomes dark with decrease in x from $x = 1.6$ to 0.6 due to the parts of Co^{2+} are oxidized to Co^{3+}. With further decrease in x, the image becomes bright again due to the oxidation process of Fe^{2+} to Fe^{3+} [24]. We further confirmed the macroscopic PS is absent at much higher rate (= 62 C).

Figure 5.7 shows the distributions of linear expansion ($\Delta L/L$) coefficient between $x = 1.6$ and 1.4 in LCoF90 film ($d = 0.5$ μm). We evaluated $\Delta L/L = -0.002 \pm 0.006$ and observed no detectable displacement in the in-plane direction.

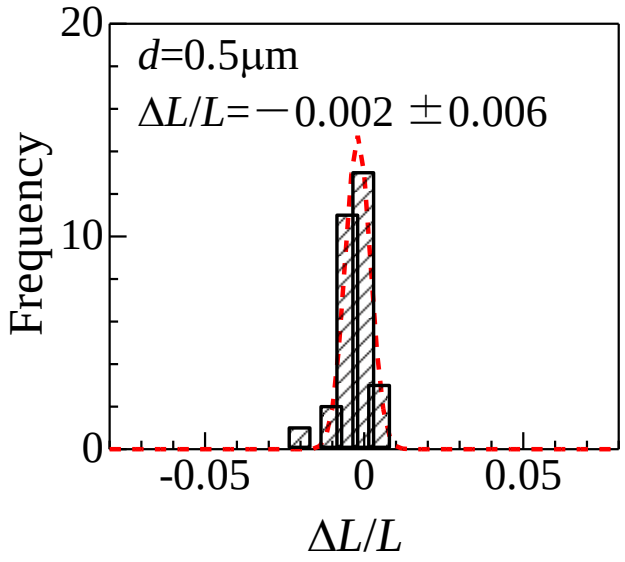

Figure 5.7 Distributions of linear expansion ($\Delta L/L$) coefficient between $x = 1.6$ and 1.4 in LCoF90 film ($d = 0.5$ μm). The broken curves represent the results of Gauss fitting. Data were cited and modified from Ref. [35].

5.1.5 Normalized absorption intensity against x

In order to investigate the macroscopic PS dynamics in more detail, we quantitatively evaluated the absorption intensity against Li^+ concentration x. Figure 5.8 shows the schematic illustration of visible absorption spectroscopy. The absorption intensity $I(x)$ at x is expressed as

$$I(x) = -\frac{1}{d} \times \ln\left[\frac{T(x)}{T_0}\right]$$

where d, $T(x)$ and T_0, are the film thickness, transmitted light intensity at x and incident light intensity. The 540 nm absorption band is ascribed to the charge transfer from Fe^{2+} to the neighboring Co^{3+}. Thus, we considered that all Co^{2+} is oxidized to Co^{3+} at $x = 0.6$, and the absorption intensity $I(x)$ at $x = 1.6$ ($Li_{1.6}Co^{2+}[Fe^{2+}(CN)_6]_{0.90}$) and at $x = 0.6$ ($Li_{0.6}Co^{3+}[Fe^{2+}(CN)_6]_{0.90}$) should be minimum and maximum, respectively. Then, we defined normalized absorption intensity (I_n).

$$I_n = \frac{I(x) - I(x=1.6)}{I(x=0.6) - I(x=1.6)} = \frac{\ln T(x) - \ln T(x=1.6)}{\ln T(x=0.6) - \ln T(x=1.6)}$$

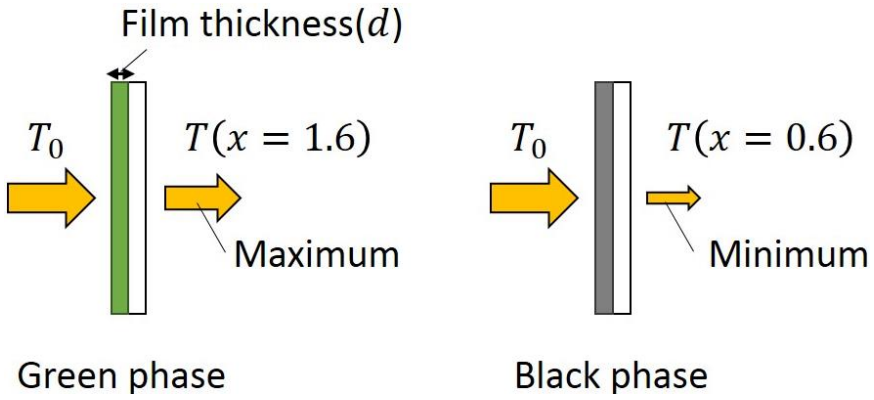

Figure 5.8 Schematic illustration of visible absorption spectroscopy.

Here, let us assume a homogeneous Co oxidation in the x range of $0.6 < x < 1.6$ and a homogeneous Fe oxidation in the x range of $0.0 < x < 0.6$ (mean-field model). In this model, I_n is expressed as $1.6 - x$ $(0.6 < x < 1.6)$ and $x + 0.4$ $(0.0 < x < 0.6)$, because I_n is proportional to the probability to find the Co^{3+} site adjacent to the Fe^{2+} site. The red lines in Figure 5.9 (a), (b) are results of the mean-field model.

Figure 5.9 (a) shows I_n against x of the thick film ($d = 1.5$ μm) in the black (A), phase boundary (B), and green (C) regions. To increase the signal-to-noise (SN) ratio,

the chromaticity was averaged within the $2 \times 2\ \mu m^2$ area (8×8 pixels) around each position, as indicated by squares in Figure 5.9 (c). In the x range of $0.6 < x < 1.6$, the I_n-x curves show significant position dependence and seriously deviate from the mean-field model. In the x range of $0.0 < x < 0.6$, however, the I_n-x curves overlap to each other and obey the mean-field model. In the black region (A), I_n steeply increases to ~ 1 with decrease in x below $x = 1.2$, indicating selective Li deintercalation and transformation into the black phase. The increase in I_n gradually saturated below $x = 1.2$, indicating that the black region covers the entire $2 \times 2\ \mu m^2$ area. In the green region (C), I_n remains nearly zero in the x range of $1.0 < x < 1.6$. With further decrease in x, I_n steeply increases to ~1, indicating that the phase boundary reaches the square position. In the boundary region (B), I_n shows an intermediate behavior between two limiting cases. Figure 5.9 (b) shows the I_n-x curve of the thin film ($d = 0.5\ \mu m$). The curve nearly obeys the mean-field model (red lines) in the entire x region, indicating that Co^{2+} is homogeneously oxidized in the thin film.

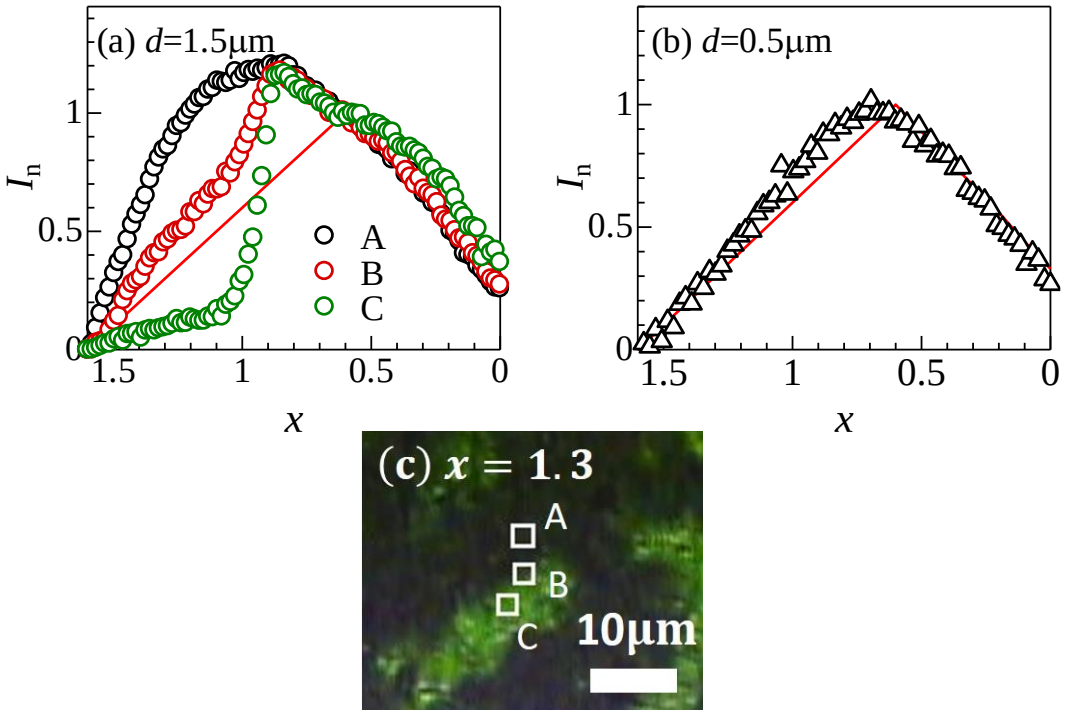

Figure 5.9 Normalized absorption intensity (I_n) of the LCoF90 film against x: (a) $d = 1.5\ \mu m$ and (b) $d = 0.5\ \mu m$. The red lines are results of the mean-field model (see text). (c) Microscopic image of thick film ($d = 1.5\ \mu m$) at $x = 1.3$, together with the investigated square positions ($2 \times 2\ \mu m^2$area). Data were cited and modified from Ref. [35].

5.2 Discussion

Let us consider the main driving force of the macroscopic PS. As shown Figure 5.3, the Li deintercalation transforms the green phase ($Li_{1.6}Co^{2+}[Fe^{2+}(CN)_6]_{0.90}$) to the black phase ($Li_{0.6}Co^{3+}[Fe^{2+}(CN)_6]_{0.90}$) and expands the black region with decrease in x. The length scale (several tens of μm) of the PS is much longer than that (several hundreds of nm) of the grain size of the film (see Figure 2.13 and 2.14). We consider the volume contraction at the phase transformation into the black phase is the main driving force of the macroscopic PS. We evaluated linear expansion ($\Delta L/L$) coefficient of black region ($\Delta L/L = -0.013 \pm 0.012$) and green region ($\Delta L/L = -0.004 \pm 0.013$), and we observed around 1 % contraction of the lattice constant a between the black phase ($a = 10.0$ Å) and the green phase ($a = 10.2$ Å). In other words, the lattice contraction due to the phase transformation propagates beyond the length scale of gain size. Then, the lattice contraction causes a significant strain at the phase boundary due to the mismatch of the lattice constant. In such a region, the Li deintercalation and subsequent phase separation into the black phase is much easier than nucleation of a new micro-domain of $Li_{0.6}Co^{3+}[Fe^{2+}(CN)_6]_{0.90}$ in another part of the green region. Figure 5.10 shows schematic illustration of macroscopic PS in the free-standing model.

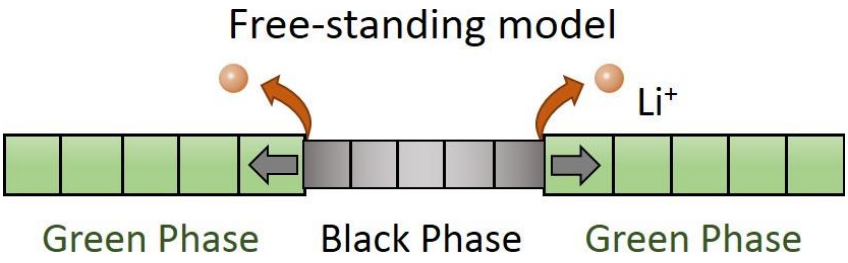

Figure 5.10 Schematic illustration of macroscopic PS. Figure was cited and modified from Ref. [35].

On the other hand, we observed no macroscopic PS in the thin film ($d = 0.5$ μm). This unexpected behavior is discussed regarding the substrate strain. Let us discuss film thickness (d) dependence of the PS dynamics. If the film were free-standing (Figure 5.10) without any constraint, the macroscopic PS would be possible even in the thin film. The actual film, however, consists of columnar crystal gains [37] and the bottom parts of the crystal gains are strongly pinned at the substrate, as schematically shown in Figure 5.11. We will call the model as “constraint model”. The thicker the film becomes, the more difficult the macroscopic PS appears due to

the constraint by the substrate (Figure 5.11 (a)). Li deintercalation occurs homogenously and does not show the PS. Similarly to the case of the thick film (d = 1.5 μm), we evaluated the distributions of linear expansion ($\Delta L/L = -0.002 \pm 0.006$) coefficient in the thin film ($d = 0.5$ μm) and observed no detectable displacement in the in-plane direction. This result means crystal gains is fixed to the substrate and cannot be deformed. In constraint model, formation of black region in the vicinity of the film surface inevitably bends the crystal pillars. To realize the macroscopic PS, the energy gain due to the phase transformation must surpass the energy loss due to the crystal pillar bending and the strain at the phase boundary. The thicker the film becomes, the less energy loss due to the pillar bending becomes, and hence the PS can occur in the thick film (Figure 5.11 (b)). Therefore, the constraint model provide a better understanding of why the PS appears in the thick film (see Figure 5.3) but is absent in the thin film (see Figure 5.6).

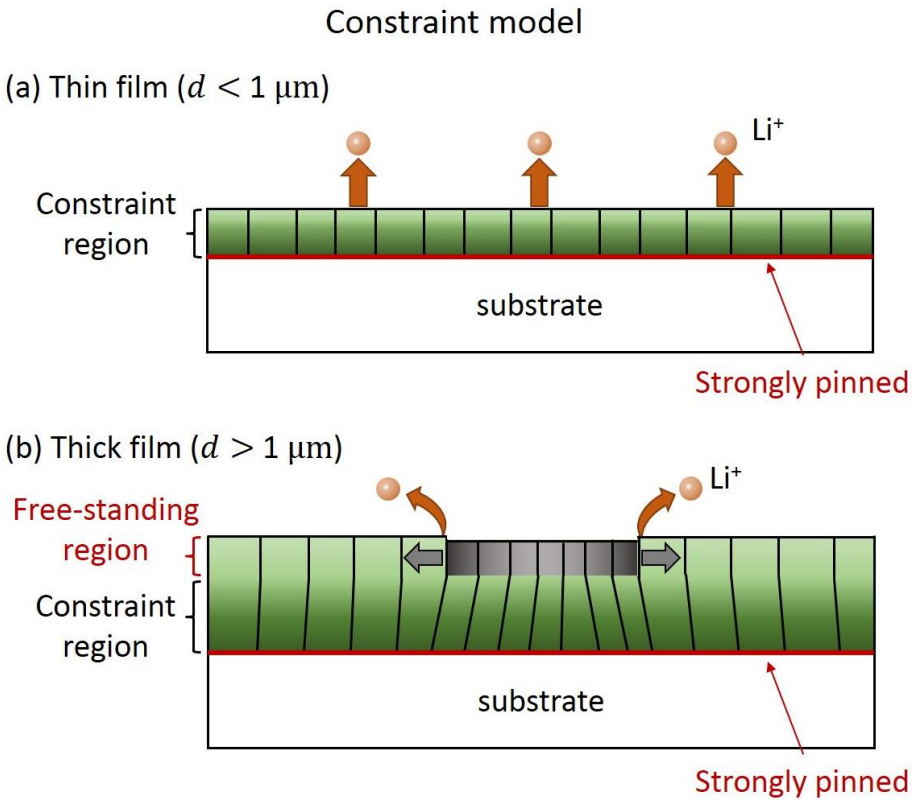

Figure 5.11 Schematic illustration of macroscopic PS in the constraint model (a) thin film, (b) thick film. Green and gray regions represents green and black phases, respectively. Figure was cited and modified from Ref. [35].

We estimated the critical thickness for the PS is order of ~1 μm, judging from the fact that the 1.5 μm film show the PS while the 0.5 μm film does not. Furthermore, we estimated the bending angle at the critical thickness film at the phase boundary. Figure 5.12 shows schematic illustration of the crystal pillars in the thick film (d = 1.5 μm). The in-plane displacement is 0.1 μm [= 10 μm (domain size of the PS) × 0.01 ($\Delta L/L$ in the black region)]. Then, the bending angle is 6 degree [= $\sin^{-1}(0.1\mu m / 1\mu m)$] at maximum. These arguments imply that the external strain due to the surrounding environment crucially influences the PS dynamics within the respective particles.

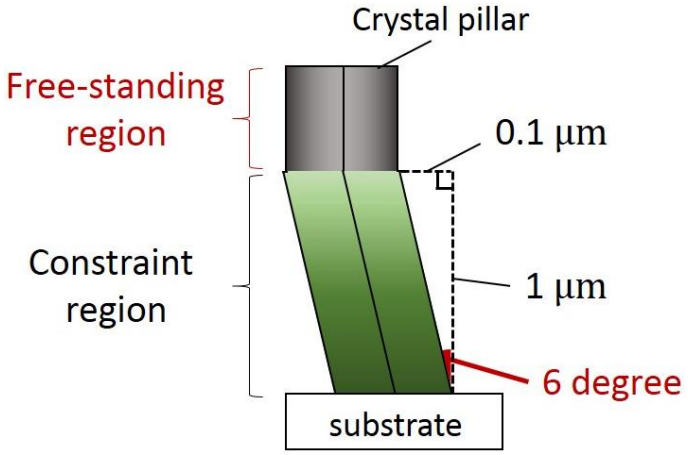

Figure 5.12 Schematic illustration of the crystal pillars in the thick film (d = 1.5 μm). Green and gray regions represents green and black phases, respectively.

5.3 Summary

In summary, we performed the *in situ* microscopic observation and found the macroscopic phase separation (several tens of μm) in thin films of $Li_xCo[Fe(CN)_6]_{0.90}$. We interpreted the volume contraction at the phase transformation is the main driving force of the macroscopic phase separation.

6 Conclusion

In this study, we investigated and discussed the interrelation between ion intercalation and structure in thin films of Prussian blue analogues. In particular, we focused on the three interrelations, (I) ion diffusion and lattice constant < chapter 3 >, (II) ion diffusion and ion concentration and ion species < chapter 4 >, and (III) ion insertion and spatial distribution of the valence of the transition metal < chapter 5 >.

In < chapter 3 >, we determined the diffusion constant D and activation energy E_a against lattice constant a in thin films of Prussian blue analogues. We found that magnitude of D (E_a) increases (decreases) with increase in a. We ascribed the decrease of E_a to the increase of framework size.

In < chapter 4 >, we determined the diffusion constant $D^{\mathrm{Na/Li}}$ and activation energy $E_a^{\mathrm{Na/Li}}$ against $x^{\mathrm{Na/Li}}$ in manganese Prussian blue analogues. We observed the steep increase of E_a^{Na} against x^{Na} in Na compound. In contrast, the increase of E_a^{Li} against x^{Li} were suppressed in Li compound. We ascribed the increase of E_a^{Na} against x^{Na} to the small number of Na^+ site.

In < chapter 5 >, we performed the *in situ* microscopic observation in thin films of cobalt Prussian blue analogues. We observed the macroscopic phase separation (several tens of μm) on the surface of film. We interpreted that the volume contraction at the phase transformation is the main driving force of the macroscopic phase separation.

Acknowledgments

This work was supported by the Mitsubishi Foundation for the Natural Sciences, Yazaki Memorial Foundation for Science and Technology, Nippon Sheet Glass Foundation for Material Science and Engineering. The elementary analysis were performed at the Chemical Analysis Division, Research Facility Center for Science and Engineering, University of Tsukuba. The synchrotron-radiation X-ray powder diffraction experiments were performed at the SPring-8 BL02B2 beamline with the approval of the Japan Synchrotron Radiation Research Institute (JASRI), at the KEK Photon Factory BL8B beamline under the approval of the Photon Factory Program Advisory Committee (Proposal No. 2014G507).

I would like to gratitude all the professors and students and persons who supported this study.

Professor Yutaka Moritomo spent enormous efforts for leading this study, and gave me critical comments from point of view of physics and scientist. I'm so grateful to Professor Yutaka Moritomo as not to be able to express my gratitude. Professor Eiji Nishibori, Professor Yasuhiro Hatsugai, Associate Professor Akinobu Kanda gave me helpful suggestions and critical reading of the manuscript. I express a deep sense of gratitude.

Assistant Professor Kazuyuki Higashiyama, Assistant Professor Wataru Kobayashi, Assistant Professor Hideharu Niwa gave me constructive comments and warm encouragements. Professor Mizuki Sakamoto, Associate Professor Hayato Kamioka (at Nihon University), Associate Professor Tamotsu Kinoshita gave me constructive comments and warm encouragements. Dr. Tomoyuki Matsuda (at Japan Automobile Research Institute) and Dr. Takayuki Shibata (at National Institute of Technology, Gunma College) gave me grateful experimental advices and supports. Mr. Kouhei Yonezawa, Mr. Syouta Akama, Mr. Yuya Fukuzumi, Mr. Rögnvaldur Líndal Magnússon, Mr. Kaoru Amaha, Mr. Shinji Iouno, Mr. Mitsuhiko Nakada, Mr. Yoshihiko Okazaki, Ms. Kyoko Kimura, Ms. Mamiko Miyama supported me in various points through a student life. I would like to express my thanks.

Ms. Katsuko Kaneko, Teacher Toru Suzuki, Teacher Satoshi Ozawa, Ms. Yukari Shinozaki and string orchestra members, Teacher Hikaru Nakano, Teacher Sugio Yamamoto, and all of the Shibatas family gave me a great deal of guidance in my private life. I would like to appreciate the warm supports.

Finally, I'm grateful to my family for their supports and encouragements in every way through my long student life. Thank you very much indeed.

References

[1] K. Mizushima, P. C. Jones, P. J. Wiseman and J. B. Goodenough, "Li_xCoO_2 ($0 < x \leq 1$): A NEW MATERIAL FOR BATTERIES OF HIGH ENERGY DENSITY", Materials Research Bulletin, **15**, 783-789 (1980)

[2] M. S. Whittingham, "Electrical Energy Storage and Intercalation Chemistry", Science, **192**, 1126-1127 (1976)

[3] J. M. Tarascon and M. Armand, "Issues and challenges facing rechargeable lithium batteries", Nature, **414**, 359-367 (2001)

[4] M. Armand and J. M. Tarascon, "Building better batteries", Nature, **451**, 652-657 (2008)

[5] A. K. Padhi, K. S. Nanjundaswamy, and J. B. Goodenough, "Phospho-olivines as Positive-Electrode Materials for Rechargeable Lithium Battries", Journal of Electrochemical Society, **144**, 1188-1194 (1997)

[6] C. Delacourt, P. Poizot, J. M. Tarascon, and C. Masquelier, "The existence of a temperature-driven solid solution in Li_xFePO_4 for $0 \leq x \leq 1$", Nature Materials, **4**, 254-260 (2005)

[7] C. Delmas, M. Maccario, L. Croguennec, F. Le Cras and F. Weill, " Lithium deintercalation in $LiFePO_4$ nanoparticles via a domino-cascade model", Nature Materials, **7**, 665-671 (2008)

[8] N. Ohmer, B. Fenk, D. Samuelis, Chia-Chin Chen, J. Maier, M. Weigand, E. Goering and G. Schütz, "Phase evolution in single-crystalline $LiFePO_4$ followed by in situ scanning X-ray microscopy of a micrometer-sized battery", Nature Communications, **6**, 6045 (2015)

[9] Hui Xia, Li Lu, G. Ceder, "Li diffusion in $LiCoO_2$ thin films prepared by pulsed laser deposition", Journal of Power Sources, **159**, 1422-1427 (2006)

[10] A. Van der Ven and G. Ceder, “First-principles theory of ionic diffusion with nondilute carriers”, Physical Review B, **64**, 184307 (2001)

[11] A. Van der Ven, G. Ceder, “Lithium diffusion mechanisms in layered intercalation compounds”, Journal of Power Sources, **97-98**, 529-531 (2001)

[12] T. Shibata, W. Kobayashi, and Y. Moritomo, ”Sodium Ion Diffusion in Layered Na_xCoO_2”, Applied Physics Express, **6**, 097101 (2013)

[13] M. Mohamedi, D. Takahashi, T. Uchiyama, M. Nishizawa, I. Uchida, ”Explicit analysis of impedance spectra related to thin films of spinel $LiMn_2O_4$”, Journal of Power Sources, **93**, 93-103 (2001)

[14] J. Xie, N. Imanishi, T. Zhang, A. Hirano, Y. Takaeda, O. Yamamoto, ”Li-ion diffusion kinetics in $LiFePO_4$ thin film prepared by radio frequency magnetron sputtering”, Electrochemica Acta, **54**, 4631-4637 (2009)

[15] T. Shibata, W. Kobayashi, and Y. Moritomo, ”Sodium ion diffusion in layered Na_xMnO_2 ($0.49 \leq x \leq 0.75$)”, Applied Physics Express, **7**, 067101 (2014)

[16] C. Ling, J, Chen, and F. Mizuno, “First-Principles Study of Alkali and Alkaline Earth Ion Intercalation in Iron Hexacyanoferrate: The Important Role of Ionic Radius”, The Journal of Physical Chemistry Communications, **117**, 21158 (2008)

[17] R. Y. Wang, C. D. Wessells, R. A. Huggins and Y. Cui, “Highly Reversible Open Framework Nanoscale Electrodes for Divalent Ion Batteries”, Nano Letters, **13**, 5748 (2013)

[18] A. Omura and Y. Moritomo, “Cs^+ Trapping in Size-Controlled Nanospaces of Hexacyanoferrates”, Applied Physics Express, **5**, 057101 (2012)

[19] T. Matsuda, J. E. Kim, K. Ohoyama, and Y. Moritomo, “Universal thermal response of the Prussian blue lattice”, Physical Review B, **79**, 172302 (2009)

[20] Y. Moritomo and H. Tanaka, “Alkali Cation Potential and Functionality in the Nanoporous Prussian Blue Analogues” Advances in Condensed Matter Physics, **2013**, Article ID 539620 (2013)

[21] T. Matsuda and Y. Moritomo, “Thin Film Electrode of Prussian Blue Analogue for Li-ion Battery”, Applied Physics Express, **4**, 047101 (2011)

[22] T. Matsuda and Y. Moritomo, “Two-Electron Reaction without Structural Phase Transition in Nanoporous Cathode Material”, Journal of Nanotechnology, **2012**, Article ID 568147 (2012)

[23] T. Matsuda, M. Takachi and Y. Moritomo, “A sodium manganese ferrocyanide thin film for Na-ion batteries”, Chemical Communications, **49**, 2750 (2013)

[24] M. Takachi, T. Matsuda, and Y. Moritomo, “Structural, Electronic, and Electrochemical Properties of $Li_xCo[Fe(CN)_6]_{0.90}2.9H_2O$”, Japanese Journal of Applied Physics, **52**, 044301 (2013)

[25] M. Takachi, T. Matsuda, and Y. Moritomo, “Cobalt Hexacyanoferrate as Cathode Material for Na^+ Secondary Battery”, Applied Physics Express, **6**, 025802 (2013)

[26] M. Takachi, T. Matsuda, and Y. Moritomo, “Redox Reactions in Prussian Blue Analogue Films with Fast Na^+ Intercalation”, Japanese Journal of Applied Physics, **52**, 090202 (2013)

[27] Y. Moritomo, M. Takachi, Y. Kurihara, and T. Matsuda, “Thin Film Electrodes of Prussian Blue Analogues with Rapid Li^+ Intercalation”, Applied Physics Express, **5**, 041801 (2012)

[28] M. Takachi, Y. Fukuzumi, and Y. Moritomo, “Na^+ diffusion kinetics in nanoporous metal-hexacyanoferrates”, Dalton Transactions, **45**, 458-461 (2016)

[29] F. Izumi, K. Momma, “Three-Dimensional Visualization in Powder Diffraction”, Solid State Phenomena, Vol. **130**, pp. 15-20, (2007)

[30] J. Bisquert, G. Garcia-Melmonte, F. Fabregat-Santiago, P. R. Bueno, “Theoretical models for ac impedance of finite diffusion layers exhibiting low frequency dispersion”, Journal of Electroanalytical Chemistry, **475**, 152-163 (1999)

[31] M. Takachi, Y. Fukuzumi, and Y. Moritomo, “Concentration dependence of Li^+ / Na^+ diffusion in manganese hexacyanoferrates”, Japanese Journal of Applied Physics, **55**, 067101 (2016)

[32] Y. Moritomo, T. Matsuda, Y. Kurihara, and J. Kim, ”Cubic-Rhombohedral Structural Phase Transition in $Na_{1.32}Mn[Fe(CN)_6]_{0.83}3.6H_2O$”, Journal of the Physical Society of Japan, **80**, 074608 (2011)

[33] Y. Moritomo, T. Matsuda, Y. Kurihara, and J. Kim, ”Cubic-Rhombohedral Structural Phase Transition in $Na_{1.32}Mn[Fe(CN)_6]_{0.83}3.6H_2O$”, Journal of the Physical Society of Japan, **85**, 038001 (2016)

[34] Y. Kurihara, H. Funashima, M. Ishida, N. Hamada, T. Mastuda, K. Igarashi, H. Tanida, T. Uruga, and Y. Moritomo, “Electronic Structure of Hole-Doped Transition Metal Cyanides”, Journal of the Physical Society of Japan, **79**, 144710 (2010)

[35] M. Takachi and Y. Moritomo, “In situ observation of macroscopic phase separation in cobalt hexacyanoferrate film”, Scientific Reports, **7**, 42694 (2017)

[36] M. Takata, E. Nishibori, K. Kato, Y. Kubota, Y. Kuroiwa, M. Sakata, “HIGH RESOLUTION Debye-Scherrer CAMERA INSTALLED AT SPring-8”, Advances in X-ray Analysis, **45**, 377-384 (2002)

[37] T. Shibata and Y. Moritomo, “Electronic Properties of All Solid Ion-Transfer Device Fabricated with Transition Metal Cyanide Films”, Japanese Journal of Applied Physics, **49**, 094101 (2010)

Related publications of this thesis

< Chapter 3 >

M. Takachi, Y. Fukuzumi, Y. Moritomo, "Na^+ diffusion kinetics in nanoporous metal-hexacyanoferrates", Dalton Transactions, **45**, 458-461 (2016)

< Chapter 4 >

M. Takachi, Y. Fukuzumi, Y. Moritomo, "Concentration dependence of Li^+ / Na^+ diffusion in manganese hexacyanoferrates", Japanese Journal of Applied Physics, **55**, 067101 (2016)

< Chapter 5 >

M. Takachi and Y. Moritomo, "In situ observation of macroscopic phase separation in cobalt hexacyanoferrate film", Scientific Reports, **7**, 42694 (2017)